Application of electron and ion beam analysis techniques to microelectronics

by T. S. Kuan
P. E. Batson
R. M. Feenstra
A. J. Slavin
R. M. Tromp

The application of electron microscopy, scanning tunneling microscopy, and medium-energy ion scattering to microelectronics is reviewed. These analysis techniques are playing an important role in advancing the technology. Their use in the study of relevant phenomena regarding surfaces, interfaces, and defects is discussed. Recent developments and applications are illustrated using results obtained at the IBM Thomas J. Watson Research Center. Potential advances in the techniques are also discussed.

Introduction

The continuing miniaturization of microelectronic devices and circuits has demanded an increasing level of sensitivity in the probing of relevant surfaces, interfaces, and defects. At present there are several powerful characterization techniques for doing so; each provides unique capabilities. A combination of them is frequently required.

Transmission electron microscopy, with its atomic-level resolution, is best suited for studying interface morphology, process-induced defects, and failure mechanisms. By using a small probe in a scanning transmission electron microscope, the chemical and electronic nature of very small regions near interfaces and defects can be examined (by electron energy loss spectroscopy). The scanning tunneling microscope can currently provide a fairly large-scale view of surface features, and by imaging at high temperatures can also provide information regarding the dynamics of relevant atom motion and crystal growth. For the study of epitaxial growth, and interfacial reactions and relaxation, medium-energy ion scattering offers a good combination of mass and depth resolution, *in situ* probe flexibility, and integration with other surface science characterization techniques.

This paper provides an overview of the application of these techniques to microelectronics. State-of-the-art capabilities and potential future developments are

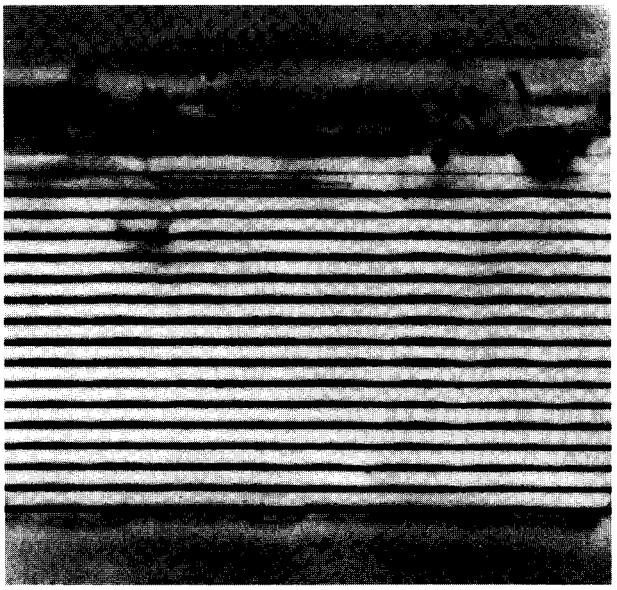

Figure 1

A cross-sectional bright-field ($\bar{1}10$) TEM image of a $Si_{0.5}Ge_{0.5}$ (6 nm)/Si (14 nm) superlattice grown on a (001)-oriented Si substrate at 580°C and then annealed at 450°C for 30 minutes. The SiGe layers, appearing in dark contrast, exhibit substantial surface undulations. From [3], reproduced with permission.

examined. The applications of the techniques to materials used in semiconductor devices and circuits are illustrated by studies recently carried out by the authors and their colleagues.

Transmission electron microscopy

The advantage of transmission electron microscopy (TEM) over other characterization techniques has always been that it can be used to image the structure of a sample in real space over a wide range of magnifications (100 times to over a million times), and to simultaneously probe local atomic arrangements in reciprocal space by selected-area diffraction. For the study of crystal defects, the high spatial resolution of TEM is particularly useful, since individual defects can be seen and their interaction can be studied. TEM has played a pivotal role in the accumulation of our knowledge of defects such as dislocations and grain boundaries, and how such defects affect materials properties. With the advent of cross-sectional sampling techniques, TEM has become even more powerful for analyzing three-dimensional structures. A cross-sectional image of a semiconductor device can reveal extended defects generated during fabrication, and can provide invaluable information regarding potential failure mechanisms. For the development of microelectronic fabrication processes such as dry etching or epitaxial growth, TEM observations are crucial in determining process-parameter sensitivities of etch/growth rate, layer morphology, and defect density.

The image resolution of TEM is limited mainly by the spherical aberration of its objective lens [1, 2]. It can be improved by increasing the electron acceleration voltage, which shortens the electron wavelength. In the last decade, medium-voltage electron microscopes (300–400 keV) have become popular because of their higher penetration power and spatial resolution. Although these modern microscopes use a standard LaB_6 cathode as an electron source, much brighter field-emission sources are becoming available. Their electron optical systems are controlled by microprocessors, and software has been developed for associated image acquisition, processing, and interpretation.

With a high-resolution objective lens pole piece, a 300–400-keV microscope can have a theoretical resolution approaching 0.15 nm. However, this limit is seldom achieved in images of real structures because of the image-overlapping problem in a three-dimensional object and the complications brought about by the highly dynamical nature of electron scattering. The practical resolution is thus dictated by how thin a sample can be prepared and by the size of the objective aperture used for imaging the sample. When a small aperture is used, permitting only the transmitted beam to form a bright-field image, the spatial resolution is low but the mass contrast between different materials is high. One can tilt the incident electron beam and use a small aperture to obtain a dark-field image of a second phase, or to image a lattice defect away from the Bragg orientation in order to narrow its strain contrast. A large aperture is used for high-resolution imaging, such as lattice imaging, which is achieved by admitting the transmitted beam and many scattered beams. As is discussed later, a lattice image can reveal the presence of lattice defects and, in favorable cases, the atomic arrangement around the defects. However, because of multiple scattering, the interpretation of a lattice image can be complicated, and precise knowledge of sample thickness and imaging conditions is often required. For disordered or amorphous materials, high-resolution TEM has been much less useful thus far, primarily because of the difficulty in overcoming image overlapping as their highly disordered structures are projected onto a two-dimensional image.

In the following sections we illustrate some of these imaging and diffraction techniques using examples from our recent studies of SiGe and Si epitaxial layers and polymer thin films grown or spun onto Si wafers.

- *SiGe/Si hetero-epitaxy and ordering in SiGe*

In a bright-field image, a sample area consisting of heavier elements, which are relatively strong electron scatterers,

tends to exhibit a darker contrast. This is true if the sample is thin enough that the contribution from multiple scattering is small. **Figure 1** shows, as an example, a bright-field image of a $Si_{0.5}Ge_{0.5}$/Si superlattice with an overlying, thick $Si_{0.5}Ge_{0.5}$ layer. The layers of the superlattice were grown on a (001) Si substrate by molecular-beam epitaxy at 580°C [3]; they are good single crystals with a low dislocation density except at the interface between the superlattice and the overlying SiGe layer. The mass contrast between the SiGe and the Si layers is quite high, permitting a detailed study of the interface morphology. Interestingly, this bright-field image indicates that the surface of each thin SiGe layer, strained in the superlattice, is not flat, but instead, undulated. The wavelength of the undulation is about 100 nm and its amplitude about 2 nm; the undulation may serve to relieve part of the 2% compressive strain in the SiGe layers during growth. The next Si layer flattens the growth surface until surface undulation reappears during the subsequent SiGe growth. The wavelength and phase of the SiGe surface undulation tend to follow that of the previously grown SiGe, indicating the effect of strain field from that underlying, buried layer. The formation of surface undulation may require a high surface mobility, since the same superlattice structure grown at a lower temperature (400°C) exhibits smooth SiGe and Si layers without any surface undulation [3].

Another interesting phenomenon regarding SiGe epitaxial growth is the onset of alloy ordering. Ourmazd and Bean [4] and LeGoues et al. [5] have reported the presence of a long-range ordered structure along the ⟨111⟩ directions in SiGe layers grown under certain conditions. **Figure 2** shows an electron diffraction pattern from such an ordered SiGe layer. Extra reflections at 1/2{111} indicate an ordering along the ⟨111⟩ direction with a periodicity of $2d_{111}$. The stacking sequence of atomic planes (which are denoted as A, a, B, b, C, c) along the ⟨111⟩ direction in the crystalline structure of a diamond can be represented as A–aB–bC–cA–a. In the projection along the ⟨111⟩ direction, the A and a planes superimpose, as do the B and b planes and the C and c planes. Furthermore, the spacing between the A and a planes is three times that between the a and B planes. Two ordered stacking sequences can be constructed with a $2d_{111}$ periodicity: Si–SiGe–GeSi–SiGe–Ge (type I) or Si–GeGe–SiSi–GeGe–Si (type II). Both types should give rise to the same set of extra reflections, but the intensity distribution among them should be different. LeGoues et al. [5] compared the observed intensities and the kinematic intensities expected from both structures, and concluded that the type II structure is the correct one. A dynamic simulation of extra reflection intensities carried out recently using the multislice method [3] indicated that as the electron energy increases and/or the degree of order decreases, the effect of multiple scattering becomes less important. **Figure 3** shows the simulated amplitudes of extra reflections from both type I and type II structures with a degree of order $S = 0.1$ versus sample thickness. The degree of order $S = 0.1$ implies that 55% of the Si and Ge sites are occupied by the preferred atoms. By comparing the simulated intensities in Figure 3 with the observed intensities in Figure 2, we were able to verify that the type II structure is in closer accord with the observations than the type I structure—because the latter would give rise to much stronger intensities at $\frac{1}{2}\frac{1}{2}\frac{\bar{3}}{2}$ and $\frac{3}{2}\frac{3}{2}\frac{3}{2}$ than at $\frac{1}{2}\frac{1}{2}\frac{1}{2}$. The origin of SiGe alloy ordering has been speculated upon in the literature. Our TEM observations found no ordering in SiGe layers grown on (111) and on (110) Si surfaces at relatively high or low temperatures [3], indicating that the occurrence of ordering is linked to the growth kinetics of the (100) surface, as suggested by LeGoues et al. [6], rather than to the epitaxial strain [7].

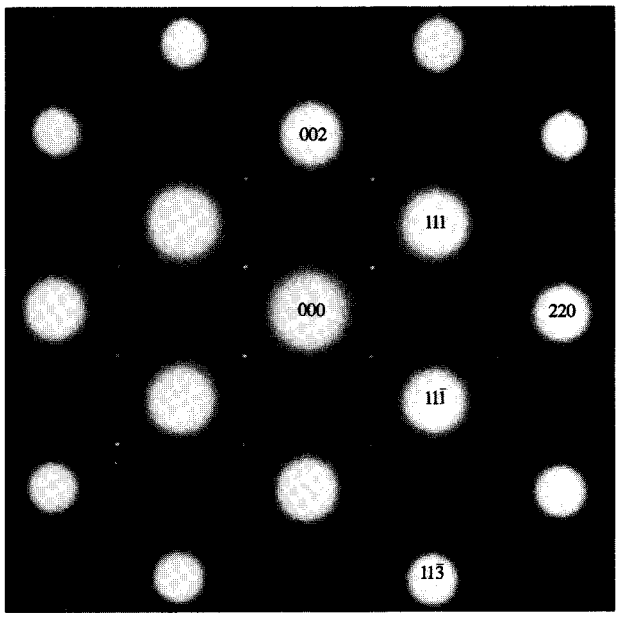

Figure 2

An electron diffraction pattern from a thick $Si_{0.5}Ge_{0.5}$ layer grown at 400°C on a (100) Si surface. Extra reflections at 1/2{111} indicate the presence of long-range order. From [3], reproduced with permission.

• *Low-temperature Si epitaxy by atmospheric-pressure chemical vapor deposition*

The Si epitaxial growth temperature using atmospheric-pressure chemical vapor deposition (APCVD) has been steadily reduced in the last few years to temperatures as low as 600°C. Blanket and selective Si epitaxy at atmospheric pressure is now achieved at low temperatures

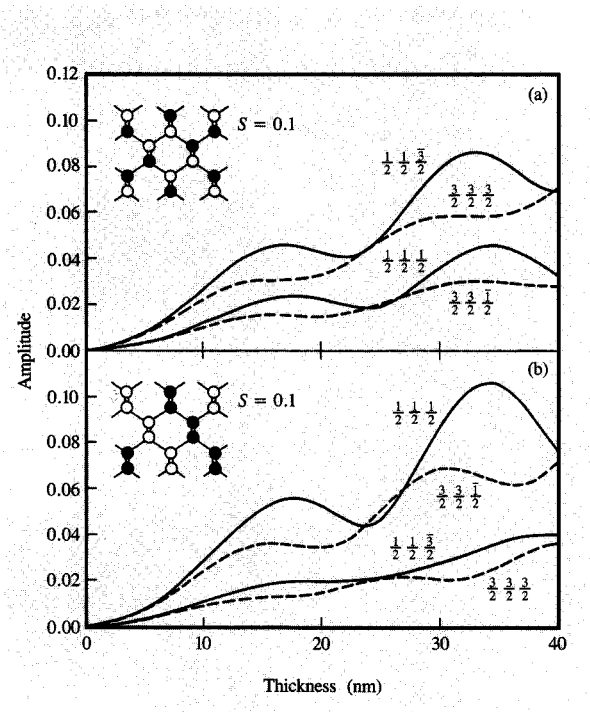

Figure 3

Simulated amplitudes of superstructure reflections (a) from a partially ordered ($S = 0.1$), type I structure; (b) from a type II structure. The amplitudes were simulated by the multislice method, assuming the use of 400-keV electrons. The preferred sites for Si and Ge atoms in the ordered structures are depicted by white and black circles, respectively. From [3], reproduced with permission.

through purification processes which exclude O_2 and H_2O impurities from the deposition zone [8]. In addition to maintaining the deposition system in an ultraclean state, the initial Si growth surface must be sufficiently free of surface oxide in order to achieve a low defect density in the epitaxial layer. Previous experiments have shown that the presence of a small amount of surface oxide leads to generation of extended defects [9]. Therefore, an effective surface cleaning process is as important as an oxygen-free environment for achieving perfect epitaxy at low temperatures.

Figure 4 shows a typical cross-sectional bright-field TEM image of an epitaxial Si layer grown from silane at atmospheric pressure at 750°C on a Si wafer patterned with thick oxide islands. Because of the nonselective nature of the growth, twins are nucleated from the oxide side walls, and the deposited layer turns into a polycrystalline structure above the thick oxide. In the image, a trace amount of residual surface oxide decorates and defines the film–substrate interface. The oxide appeared as discrete islands when imaged at higher magnifications. To study the defect mechanism associated with the surface oxide, use was made of an ultraclean, load-locked APCVD system [8]; prior to Si deposition, the Si substrate surface was first cleaned of any residual oxide and then exposed to H_2 and argon carrier gases containing trace amounts of oxygen (25 to 100 ppb) at 650–750°C for various lengths of time. When surface oxide is introduced in a controlled manner, the density of defects increases by several orders of magnitude ($10^3/cm^2$ to $10^8/cm^2$) as the surface oxygen content increases from $10^{12}/cm^2$ to $5 \times 10^{14}/cm^2$ [9]. Cross-sectional TEM lattice images of these samples revealed that defect formation is directly related to oxide island size. When the oxide islands are small, growth can occur over them without generating any defects in the epitaxial layer as in Figure 4; at larger oxide islands, twins are nucleated, as shown in **Figure 5(a)**. Microtwins are the dominant defects induced by the surface oxide. In some cases, a misoriented grain can also form on a large oxide island, as shown in **Figure 5(b)**.

High-resolution TEM observations indicate that for each growth condition, only those oxide islands larger than a critical size lead to defect formation [10]. This critical island size is strongly dependent on the growth temperature and the reagents used. The density of twins in the epitaxial layer tends to decrease with higher deposition temperatures, and twins form more readily if use is made of dichlorosilane rather than silane. Our measurements over more than 100 oxide islands have indicated that the critical size for triggering twin formation is about 6 nm using dichlorosilane and about 30 nm using silane (at 650°C). Twins formed during growth using dichlorosilane usually extend throughout the entire epitaxial layer, while defects formed on the oxide islands if silane is used can be either microtwins or misoriented nanocrystals, all of which are terminated within about 10 nm of growth.

- *Imaging of polymer materials*

Polyimides are well-suited for use as insulators in on-chip interconnection and in packaging because of their high thermal stability, low dielectric constant, good mechanical strength, and resistance to moisture. These polymers are usually highly disordered, and spin-on techniques are most often used to apply films of them onto substrates. The films exhibit substantial anisotropy in their structural, electrical, and mechanical properties. Understanding and control of their anisotropy have been important in adapting them to chip and packaging applications.

Thus far, the structure of polyimide films has been investigated mostly by optical and X-ray or electron diffraction techniques. Direct imaging by TEM at high magnifications has not been explored extensively because the overlapping of the local structure in a specimen of a given thickness gives rise to a granular contrast, which

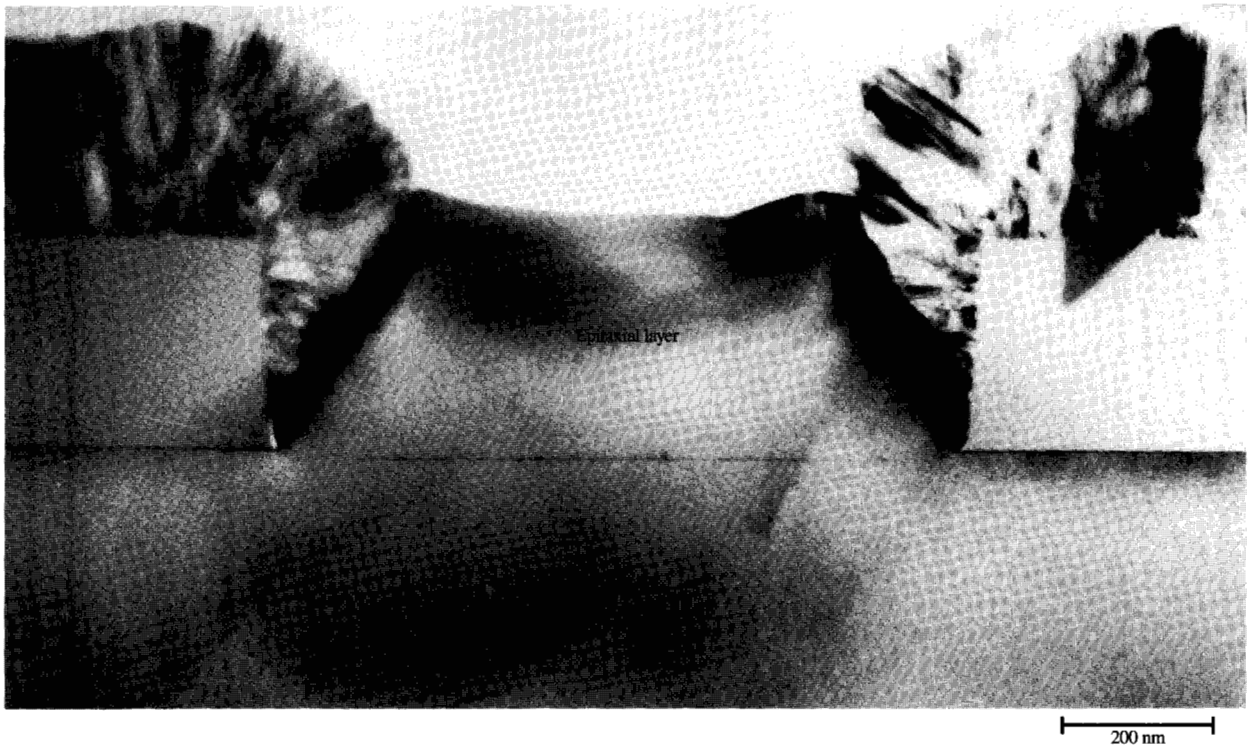

Figure 4

A cross-sectional bright-field TEM image of a Si layer grown from silane at atmospheric pressure at 750°C on a (100) Si wafer patterned with 280-nm-thick SiO_2 islands. A trace amount of surface oxide was present at the epitaxial layer–substrate interface.

bears little useful structural information. With regard to polyimides such as spun-on BPDA–PDA or others synthesized by the layer-by-layer method, if the TEM specimen is very thin (e.g., less than 5 nm thick), local structures at the molecular level can be directly imaged [11]. The polyimides examined were found to be stable enough structurally to withstand the 200-keV electrons used during TEM observation.

Figure 6 shows a cross-sectional bright-field TEM image of a 100-nm-thick BPDA–PDA film that was spun onto a Si substrate. The image was obtained using a large objective aperture of 0.024 rad semi-aperture angle. In sample areas thinner than 5 nm (e.g., area A), lattice fringes from small regions 1.5 to 2 nm in size were observed, indicating the presence of local crystallization in the film. This local ordering was not obvious in thick areas (e.g., area B) because of image overlapping. The orientations of these crystalline regions closer to the substrate tended to align roughly along the substrate surface and became more random away from the film–substrate interface. Similar local ordering was also observed in images of polyimide PMDA–ODA.

Interest in the high-resolution TEM imaging of polymers is increasing. Lattice imaging has been used to study crystalline polymers [12]. Further improvements in the spatial resolution and the efficiency in collecting scattered electrons for low-dose imaging should soon make TEM a viable approach for studying such materials [13, 14].

Scanning transmission electron microscopy

In TEM, a set of high-quality electron lenses is used to form a magnified image of an area of the sample. One image point at a detector corresponds to a single point at the sample. In scanning transmission electron microscopy (STEM), the connection between a sample point and the image is achieved by forming a relatively small probe of electrons and scanning it in a raster fashion across the sample, as shown in **Figure 7** [15–17]. Extended STEM detectors can be used to measure scattering intensity at particular angles or ranges of angles. With suitable equipment, the energy lost by the probe electrons can be measured for particular specimen positions. Use can also be made of detectors designed for detecting X-rays, specimen current, luminescence, etc.

In a simplified sense, STEM is similar to TEM, because the probe-forming electron optical system used in STEM is similar to the image-forming system used in TEM. Referring to Figure 7, if an electron ray diagram is drawn

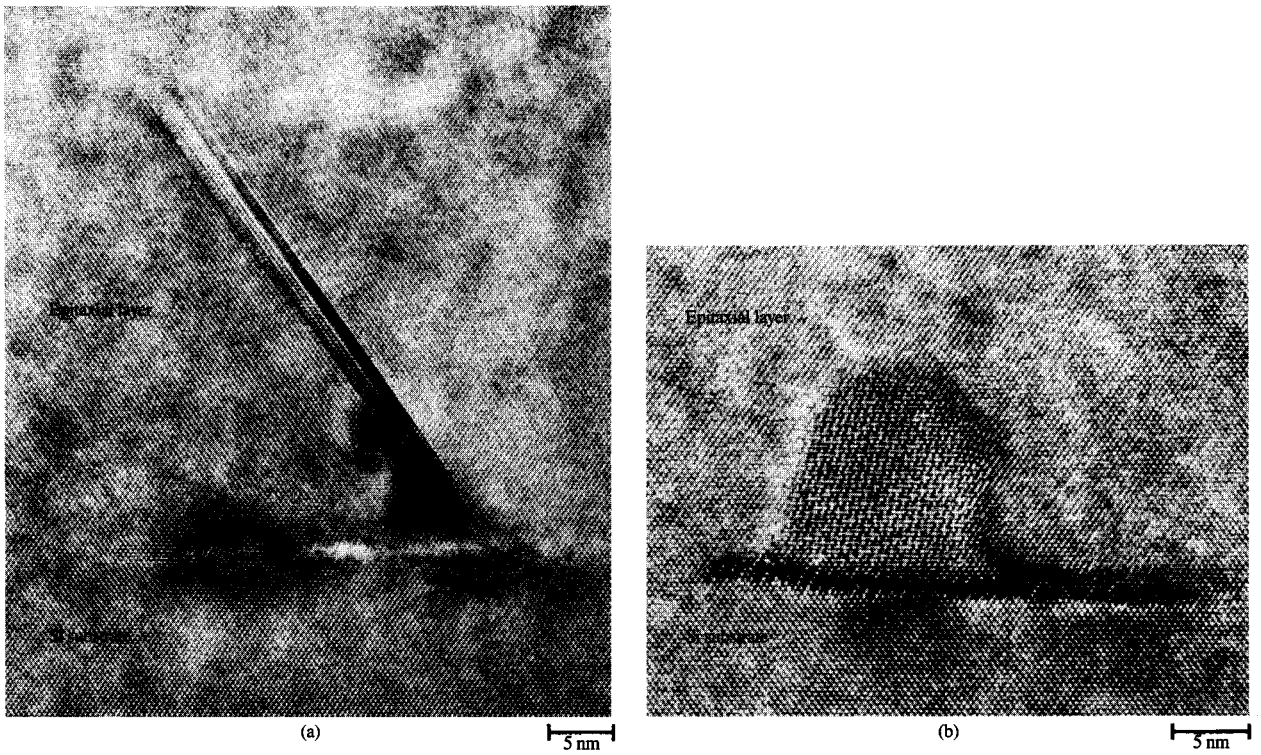

Figure 5

Cross-sectional TEM lattice images of (a) a microtwin and (b) a misoriented nanocrystal formed at surface oxide islands during growth at 650°C using silane.

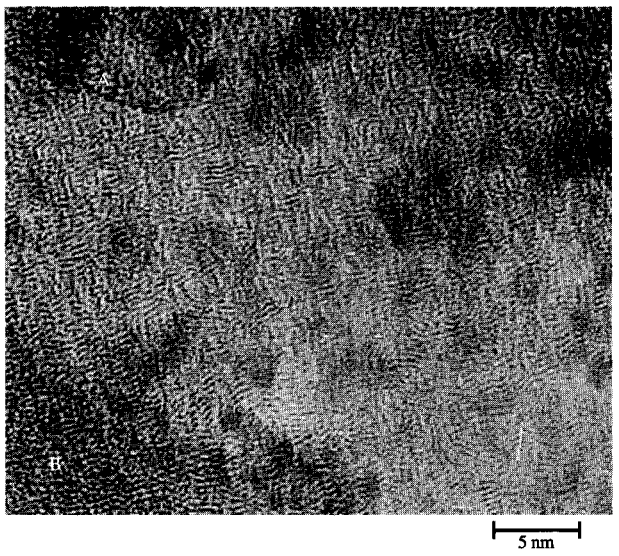

Figure 6

A cross-sectional bright-field TEM image of a BPDA–PDA film spun onto a silicon substrate. The film contained small ordered regions 1.5 to 2 nm in size aligned roughly along the substrate surface. From [11], reproduced with permission.

for the TEM, an equivalent STEM diagram can be constructed by reversing the direction of the electron propagation, replacing a TEM image point at the screen with an electron source. At the specimen plane, the source is imaged with a large demagnification to produce a small spot. The spot is scanned to other specimen locations by magnetic deflection coils. The different types of detectors are positioned in front of or behind the sample depending on the nature of the particular signal to be examined. Figure 7, for example, shows detector locations for energy-dispersive X-ray (EDX) analysis, electron energy loss spectroscopy (EELS), and annular dark-field (ADF) imaging.

With the advent of practical field-emission electron sources, STEM became a very interesting imaging technique. Useful high-resolution imaging in most materials requires spatial resolutions of order 0.2–1 nm. In order to obtain a reasonable current into a probe of this size, a source of very high brightness is necessary. The field-emission source gives about four orders of magnitude (10^9 A/cm^{2}ster) more brightness than the more common LaB_6 thermionic emitter. Thus, a current of 1–5 nA into a 0.5-nm probe is possible.

We now discuss briefly two STEM techniques which promise to be particularly useful for studies in

semiconductor materials: annular dark-field imaging and spatially resolved electron energy loss spectroscopy (EELS).

• *Annular dark-field imaging of a Ge-rich layer in Si*

When electrons pass close to the nucleus of an atom, they are electrostatically deflected through a large angle (classical Rutherford scattering). The scattered electrons can be collected with an annulus detector located behind the specimen, as shown in Figure 7. If its inner diameter is large enough, small-angle beams—the direct unscattered beam, crystalline diffraction beams, and most of the inelastically scattered electrons—are excluded. The remaining intensity should be due primarily to electrons experiencing a single Rutherford scattering event and those that constitute a thermally scattered (diffuse) background. Because it has been found to depend strongly on the atomic number of the scattering atoms, this type of signal has been used to image individual heavy atoms on a light atom substrate [16]. For this reason, such annular dark-field (ADF) imaging has been used extensively in the past for imaging catalyst particles.

Recently, high-resolution probe-forming electron optical systems have been used to produce 0.18–0.22-nm electron probe sizes at 100 keV. With this spatial resolution, it has been possible to image a semiconductor lattice having a periodicity of 0.3–0.4 nm. **Figure 8(a)** illustrates the use of the ADF imaging technique for examining a 3.0-nm-thick layer of Ge implanted in Si, from the work of Pennycook and Jesson [18]. The sample examined was prepared by standard sectioning in a (110) plane which was perpendicular to the interface. The [111]-oriented Si atom pairs were imaged with good contrast. The Ge-rich layer could be clearly identified using the atomic number sensitivity of the ADF imaging technique. **Figure 8(b)** shows a high-resolution TEM lattice image at optimum conditions. While the atom pairs are resolved, there is no atomic number sensitivity. As mentioned in the previous section, a bright-field TEM image can reveal substantial mass contrast from a Ge-rich layer (Figure 1), but in this case the spatial resolution is relatively poor because of the small objective aperture used.

High-resolution lattice imaging in TEM is also notoriously sensitive to the precise imaging conditions used and the specimen thickness. Reversals of contrast and nonstructural interference fringes are common. Thus, the bright dots in Figure 8(b) can correspond either to atoms or to holes, depending on the particular imaging conditions used. As a result, structural analysis can require detailed computational comparisons of many images. The ADF imaging approach does not suffer from this difficulty. The physical basis for this is interesting: Standard high-resolution images are the result of coherent summations of many diffracted waves from many atom layers within the crystal. Thus, they are inherently interference phenomena. Since the Rutherford scattering occurs only at very small distances from the atom core, the phase of the scattered electrons is sensitive to the instantaneous location of a single atom rather than to an average position defined by an ensemble of atoms within a plane. The instantaneous atom location, however, is constantly changing because of thermal vibrations. This randomizes the phase of the scattered electron, and interference effects are averaged out over the many scattering events required to form an image. Thus ADF imaging is incoherent in nature; it is generated by each atom in proportion to the electron intensity close to its site.

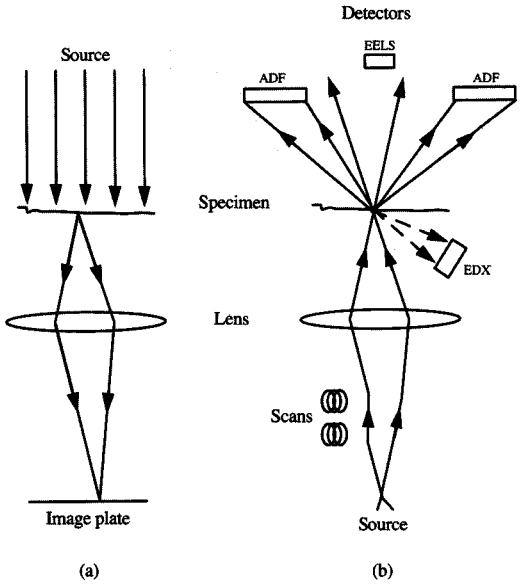

Figure 7

Comparison of (a) TEM and (b) STEM techniques. Although use is made of equivalent electron optical systems, in TEM an image is formed of the sample, whereas in STEM a small probe is scanned across the sample to generate an image. The latter permits use of detector configurations that depend on some property of the specimen other than its structure.

It is not surprising that this is the case for small numbers of atoms, but it is not obvious why the incoherent limit persists for thick, crystalline samples. It turns out that, in the case of beam orientations close to a zone axis, strong channeling of the electron beam occurs along atom columns in the crystal. If the probe electrons are described in a two-dimensional summation of crystalline Bloch waves, the first term can be shown to have a strong symmetric, s-wave symmetry about an atom column [18, 19]. It can be shown that the s-wave scattering

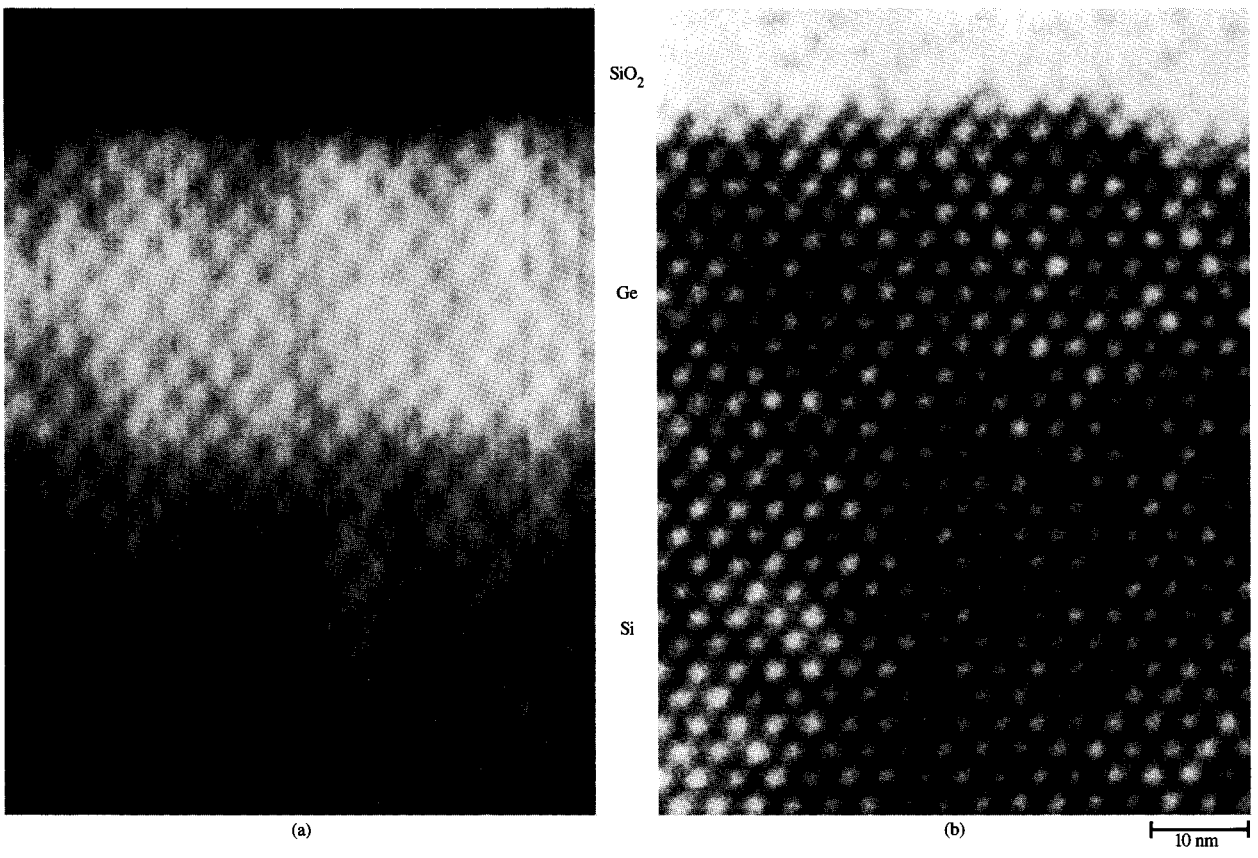

Figure 8

Images of Si implanted with Ge, taken (a) via STEM, using an annular-dark-field detector, and (b) via high-resolution TEM. Atomic number contrast is visible in (a). The lattice resolution in (a) is due to the incoherent scattering at individual atoms. The lattice resolution in (b) is due to the coherent interference of many waves. Photographs courtesy of S. J. Pennycook (Oak Ridge National Laboratory).

dominates the high-angle Rutherford scattering. It can further be shown that in this case, the probe can be thought of as a set of filamentary electron beams moving down the atom columns with intensities that are proportional to the probe intensity at the column locations. Thus, a simple convolution of the probe shape with the atom column positions serves to predict the ADF images.

Instruments are currently becoming available with probes in the 0.1-nm range. These should make it possible, e.g., to image the differences between Ga and P in GaP. Direct imaging of anti-site defects, reconstruction at buried interfaces, and layer-by-layer intermixing in multilayer materials should all become possible.

• *Spatially resolved electron energy loss scattering*

The ADF imaging technique can provide us with a detailed determination of the structural and elemental composition of a small volume of a sample, but it does not yield information about its electronic structure. One of the reasons for this is that the ADF method deliberately excludes scattering intensity at small angles, which results from interactions among atom columns. Another reason is that scattering involving electronic charge between atom columns is primarily inelastic in nature. Thus, an attractive complement to ADF imaging would be to collect electrons scattered to smaller angles and sort them out as a function of the amount of energy given up to the sample. This could provide a measure of the available electronic excitations within the sample, and thus give us information about its electronic structure.

The main difficulty here is that the relevant energy scale for the electronic structure of semiconductors is 0.1–5.0 eV. Typical probe beam energies are 100–300 keV. Thus, a spectrometer system must be capable of providing a resolving power of better than 10^{-6}. In addition, although the scattering angles are small relative to the ADF signal, they are still quite large in terms of common spectrometer designs. Therefore, the resolving power must be maintained in the face of aberrations introduced by nonideal collection angles. Means to overcome these

difficulties are being developed [20], and it has recently been possible to obtain 0.2-eV resolution spectra from 0.4-nm areas by using STEM.

There are two energy ranges of interest with regard to determining electronic structure: 1) direct interband excitations that produce scattering intensity in the 0.2–2.0-eV energy range (these carry information about both initial and final electron states, both of which lie near the Fermi level); and 2) core excitations (direct single-electron excitations from the discrete core level to the conduction bands of the material) in the range beyond 50–100 eV. Probing in both ranges yields information about the local electronic structure of a semiconductor.

• *Direct interband excitations in Si and GaAs*

The cross section for scattering in this case can be derived by comparison with optical measurements, and lies in the range from $\partial\sigma/\partial E \approx 0.1$ to 10×10^{-22} cm^2eV^{-1} [21]. This is small because most of the electronic density of states (DOS) is distributed throughout a wide band removed from the band edges. For instance, the DOS in Si at the conduction band edge is only about 0.05 $atom^{-1}eV^{-1}$. **Figure 9** shows a plot of the energy distribution in the 0–3-eV energy loss range for Si and GaAs. The interband scattering onsets are clearly visible at 1.1 and 1.4 eV, respectively. However, in the absence of monochromatization of the field-emission electron source, the intensity background from the unscattered beam is almost 100 times larger than the desired signal. This background arises from electrons which tunnel out of the field-emission tip from well below the Fermi level. It is just possible to subtract this intensity to obtain the results in **Figure 10**, showing that a fairly accurate value for the band gap can thus be obtained. This type of measurement has been used, e.g., to identify Fermi level pinning near a single misfit dislocation at a GaAs/GaInAs interface [21].

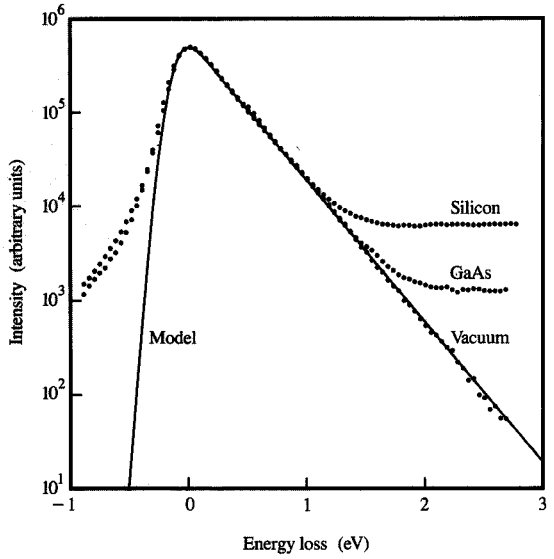

Figure 9

Electron intensity within 3 eV of the unscattered beam in a STEM system. The asymmetric profile reflects the energy distribution of electrons tunneling out of the field-emission source of the system. Direct interband scattering is shown for Si and GaAs. The scattering intensity is only about 1% of the background intensity associated with the unscattered beam.

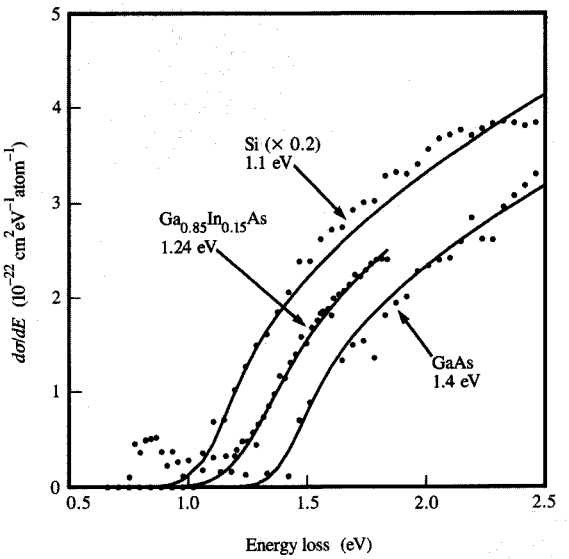

Figure 10

Results derived from the data of Figure 9, showing interband scattering for Si, GaAs, and $Ga_{0.85}In_{0.15}As$. The values for the associated band gaps can be deduced by fitting with a model having a shape that is convoluted with the instrumental resolution.

• *Core excitations in silicon, silicon oxide, and metal/silicon interfaces*

Excitations of inner core electrons into local conduction band states produce fine structure within 1–5 eV of typical core absorption edges. These can be used to deduce the atomic bonding environment by reference to "fingerprint" spectra [22]. **Figure 11** contains an image of an Al/SiO_x/Si structure that was used in an experiment to determine the local stoichiometry and structure of an SiO_x layer. The intention of the experiment [23] was to construct a 5-nm-thick layer of stoichiometric SiO_2 surrounded by layers

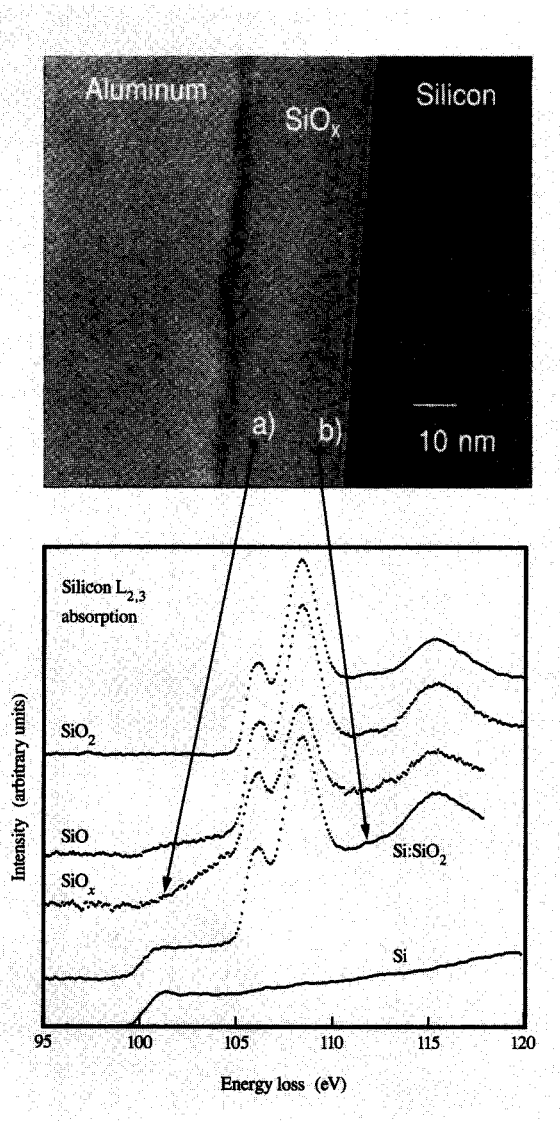

Figure 11

Summary of an experiment that was carried out to determine the local stoichiometry and structure of a SiO_x layer. Comparison spectra from standard compounds were used to interpret multicomponent and distorted spectra obtained from the specimen.

consisting of SiO_2 with small, embedded Si islands. Comparisons of the total scattering intensity of Si and O core absorption verified the desired average stoichiometry. But the distribution of Si in SiO_2 was not obtainable from average stoichiometry nor from imaging. The figure also contains comparative spectra of the Si $L_{2,3}$ edge in SiO_2, SiO, and Si. SiO_2 has a characteristic three-peaked structure which arises from transitions to final states which are bound locally within the SiO_4 tetrahedron. Thus, even for the substoichiometric oxide, SiO, a large part of the signal detected was very similar to that obtained from SiO_2. For SiO, however, some of the tetrahedra are incomplete, leading to a small ramp of scattering intensity from the SiO_2 onset down to the normal Si onset. In region a), the spectrum shows this behavior, and so it was characterized as being a uniform SiO_x mixture. In region b), the absorption could easily be decomposed into a bulk Si portion and an SiO_2 portion. This region is composed of sub-nm Si islands embedded in the SiO_2. On annealing at moderate temperatures, the absorption from region a) became identical with that of region b), confirming the desired structure.

Such investigations rely on comparisons with standard materials. This method cannot help with the investigation of electronic structure, because variations on a scale of 0.1–0.5 eV are important and may not be reproduced in a standard which differs only slightly from the area of interest. We must then try to understand and interpret spectra from first principles. In **Figure 12** we show a high-resolution example for the Si $L_{2,3}$ ($2p \rightarrow CB$) edge that shows there is some promise in this approach. The data were obtained with a 1-nm probe in Si approximately 50 nm thick. It was sharpened by unfolding the 0.4-eV-wide field-emission source to produce a Gaussian spectral resolution of 0.2 eV. The spin 3/2 portion of the $L_{2,3}$ edge was then isolated by Fourier transform techniques, assuming a spin-orbit splitting of 0.608 and a 2:1 occupation ratio for the core spins. The results obtained were compared with calculations for the total DOS, the s,d-projected final DOS [24], and the differential cross section [25]. Most of the structure could be reasonably explained by such single-electron calculations, provided the appropriate symmetry selection rules were included. This was a surprising result, since optical absorption spectra are assumed to be greatly distorted by core excitonic contributions. It turns out that EELS spectra benefit by additional core hole screening in the presence of the probe electron [26]. In silicon, this almost totally suppresses the core excitonic distortions.

We now can envision the illustrative experiment depicted by **Figure 13**. Starting with a cross-sectioned sample of an Al/Si(111) interface, if we position the electron probe far from the interface, so that the probe electrons travel parallel to the interface, we expect to observe the bulk absorption. Band bending should not be observed, because both the core-level and the conduction bands are shifted by similar amounts. As indicated in the figure, a core edge shape should be obtained which is characteristic of the bulk. If in-gap states occur at the interface, they may pin the Fermi level there. Transitions from the core level to these in-gap states should produce intensity below the bulk onset of the absorption. Measurement of the difference in onset energy of the in-

gap states and the bulk should then give a measurement of the Schottky barrier for n-type Si.

Figure 14 summarizes the results from such an experiment, using a 0.4-nm-diameter probe. Although the statistical quality was poor, the shape of the core absorption was clearly a function of the distance from the interface. Within 0.5 nm of the interface, in-gap scattering could be seen, and a Schottky barrier height of 0.6 eV could be inferred [27]. Also, variations in the shape above the edge onset were visible. These turn out to be a signature of the modification of the Si conduction bands necessitated by the pulling down of states into the gap by the presence of the Al. The behavior shown here is consistent with the metal-induced-gap-state model for Schottky barrier formation [28].

Thus, spatially resolved EELS in an STEM system can produce detailed information on the local bonding and electronic structure within the probe region. By combining this with ADF imaging, we can thus obtain a fairly complete picture of the elemental, chemical, and electronic nature of very small regions near interfaces and defects.

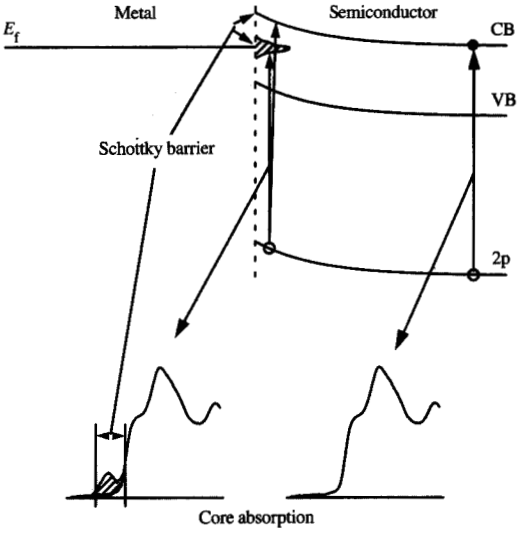

Figure 13

Schematic illustration of an energy-loss experiment near a metal/semiconductor interface. Away from the interface, even in regions influenced by band bending, the bulk absorption shape should be obtained. Near the interface, if in-gap states are present, scattering to the in-gap states should produce pre-edge intensity in the absorption. Examination of this intensity can provide a measurement of the height of the local Schottky barrier.

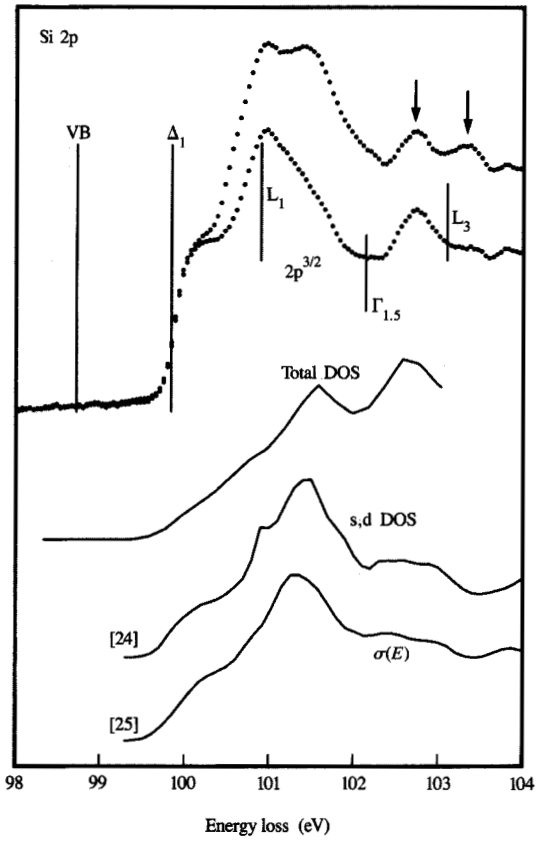

Figure 12

Comparison of measured Si L_3 core absorption with calculations. The structure observed can be accounted for on the basis of single-electron calculations.

Scanning tunneling microscopy

Since its inception in 1982, scanning tunneling microscopy (STM) has proven to be a powerful technique for the study of surfaces. Ordered arrays of atoms and disordered atomic features have been observed on many metal and semiconductor surfaces. Clean surfaces as well as isolated adsorbates and thin overlayers have been studied. The technique has been used in a variety of environments including ultrahigh vacuum (UHV), air, and various liquids, and at temperatures ranging from that of liquid helium to above room temperature.

In the years immediately following its development, much of the STM research focused on spectroscopic measurement and probing the energy levels and wavefunctions of surface states [29–31]. These studies required, in addition to the high spatial resolution characteristic of STM, the ability to selectively scan over energy levels (by varying the bias voltage between the

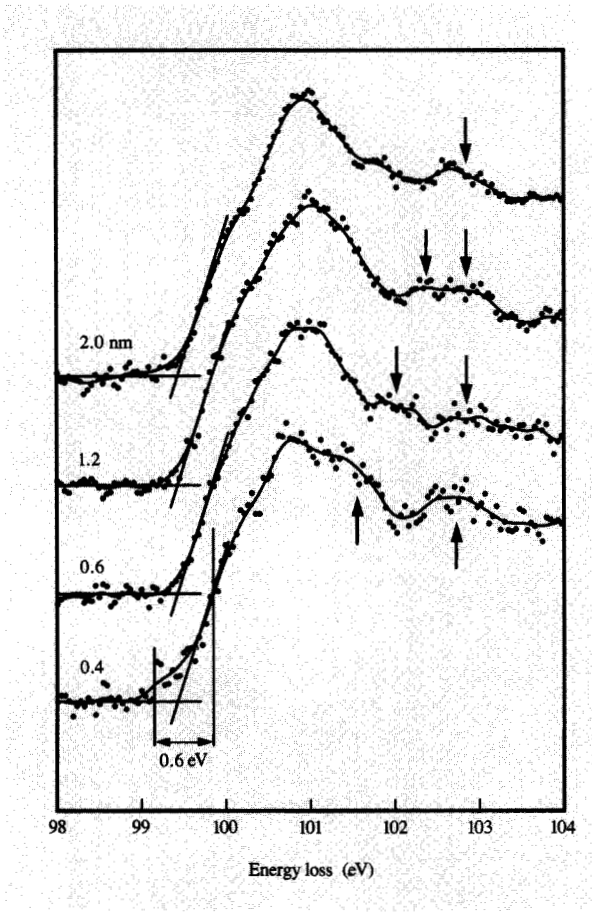

Figure 14

Associated results of Si L_3 measurements as a function of distance (0.4 to 2.0 nm) from an Al/Si(111) interface. In-gap intensity was present; additionally, distortions above the edge were visible. The Schottky barrier height could be inferred to be 0.6 eV. The overall distortion of the edge was consistent with the metal-induced-gap-state model for Schottky barrier formation.

probe tip and sample) at desired locations on the surface. For the past several years, the focus has shifted to the study of the kinetics of deposition and growth on surfaces, including the epitaxial growth of Si and Ge [32–34]. For this purpose, the acquisition of large (micron-scale) images of a surface has become necessary, while maintaining the ability to zoom in on atomic-scale features. Recently, several groups have been working on STM imaging at high temperatures, typically at several hundred degrees Centigrade [35, 36], permitting the observation of atomic motion on a surface, and thus opening up a new class of potential STM investigations.

In this section, we illustrate the latter by describing recent results obtained from the Ge(111) surface [37]. The (111) surface of germanium was chosen for these studies mainly because the temperatures required to induce atomic motion on such a surface (about 150°C) are considerably lower than required for a silicon surface. Nevertheless, the results obtained for that surface are expected to affect our knowledge of the Si surface. We first describe the structure of the Ge(111) surface, and illustrate several methods for using STM to determine it. We then present results for its high-temperature imaging. We close with a summary of our results, along with a brief discussion of other applications of STM to the study of semiconductor surfaces.

Structure of the Ge(111) c2×8 surface

The (111) surface of Ge contains *adatoms*. These adatoms, which are themselves germanium atoms, form arrangements characteristic of the (111) surface: Each adatom forms bonds to three underlying Ge atoms, leaving a single dangling bond remaining on the adatom itself. The adatoms dominate the STM images, at least for the case of positive sample bias. In **Figures 15(a)** and **15(b)** we show schematically the two simplest arrangements of adatoms on a Ge(111) surface: 2×2 and c2×4 stacking. An alternating sequence of 2×2 and c2×4 results in the c2×8 stacking arrangement [38], shown in **Figure 15(c)**. **Figure 15(d)** shows a side view of the adatom-covered surface, and also the *bilayer* of atoms below the adatoms.

The Ge(111) surfaces which were studied were prepared by first cleaving a Ge crystal to expose its (111) face, and then annealing it at temperatures near 300°C. This procedure results in the formation of large flat terraces, on which the adatoms form a centered 2×8 reconstruction. **Figure 16** shows a high-resolution STM image of such a surface. A rectangular 2×8 unit cell, measuring 27.7 × 8.00 Å, is shown in the center of the image. The atomic arrangement can be seen to form double rows extending along the $[01\bar{1}]$ direction. Each double row contains two corrugation maxima (adatoms) per unit cell, and the next double row is shifted by 1/2 unit cell in the $[01\bar{1}]$ direction. Within a single domain of the c2×8 reconstruction, the dominant type of disorder is found to be an extra row of adatoms, as shown by the arrows in Figure 16. Near this extra row, the local stacking forms a 2×2 arrangement.

The geometric structure of the c2×8 surface can be deduced by STM spectroscopic methods. From a comparison of Figure 16 with Figure 15(c), it can be seen that the observed arrangement of corrugation maxima in the STM agrees with that expected for the adatoms in the c2×8 arrangement. However, it turns out that this agreement is not sufficient to determine the structure of the surface. There exist two different structural models, both with c2×8 symmetry and identical arrangements of adatoms, but differing in the structure of the atomic layers below the adatoms. The STM method of voltage-dependent imaging (originally developed for studying Si and GaAs

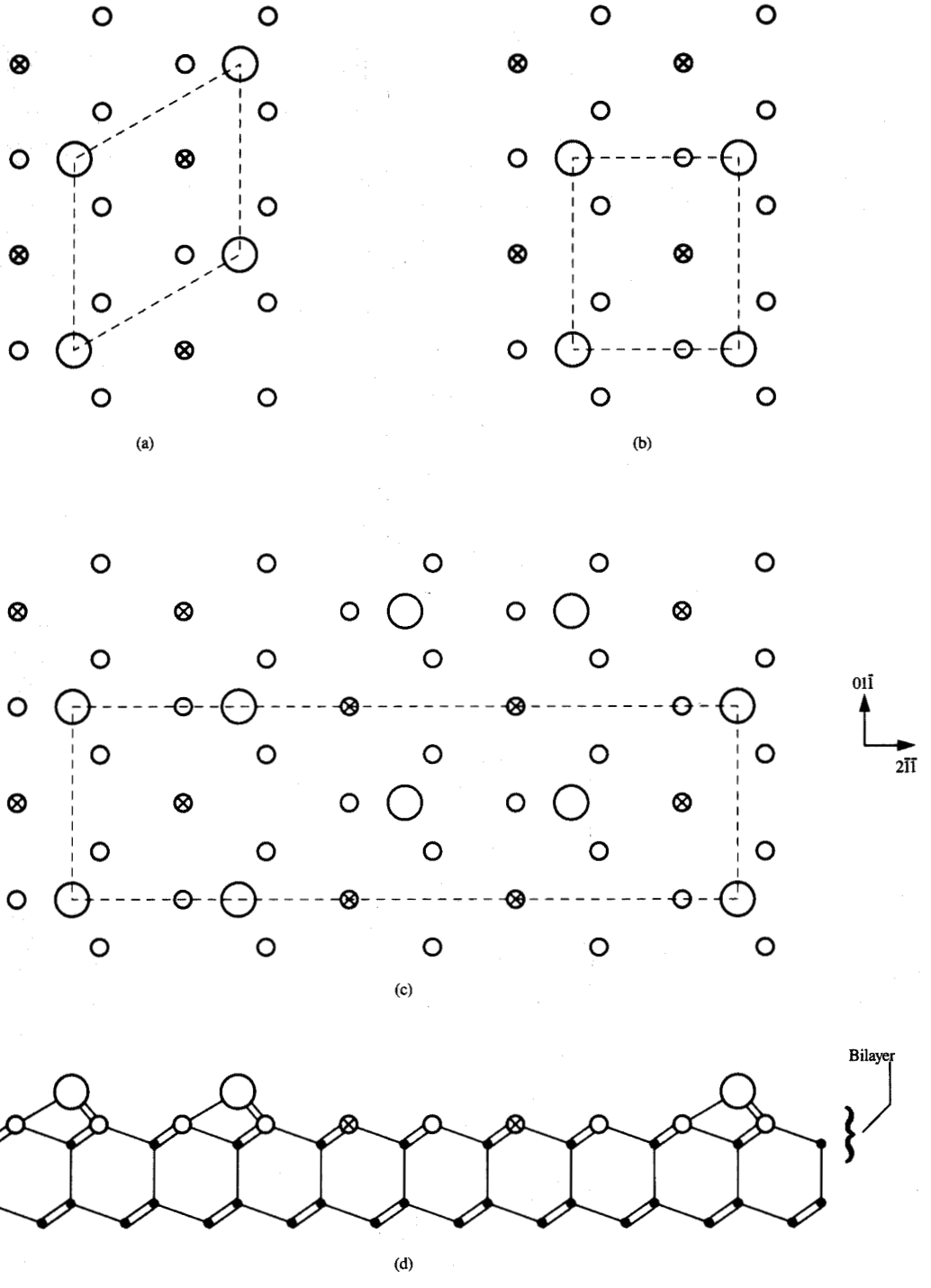

Figure 15

Schematic views of Ge adatom arrangements on a Ge(111) surface. The adatoms are shown by large white circles. Atoms in the layer immediately below the adatoms are shown by small white circles (including the rest atoms, indicated by ⊗ symbols). The underlying atoms are depicted as black dots. Parts (a)–(c) show top views of various stacking arrangements: (a) 2×2, (b) c2×4, and (c) c2×8. Minimum-size unit cells are shown by dashed lines. Part (d) shows a side view of the c2×8 adatom structure and the underlying bilayer of atoms.

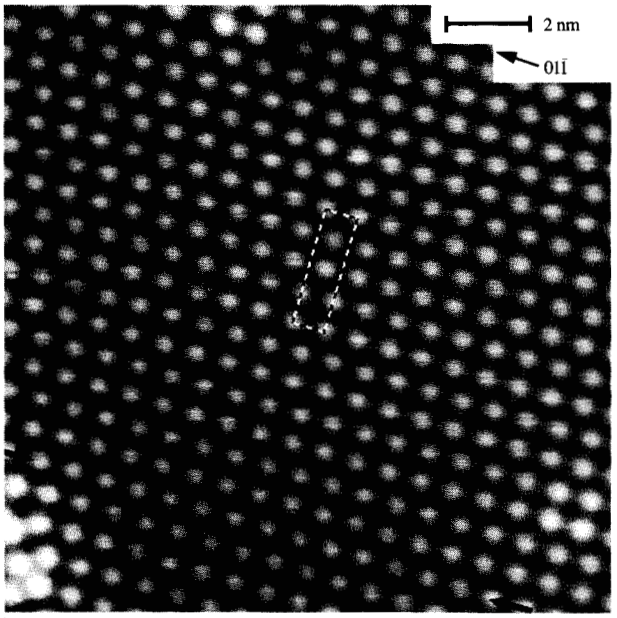

Figure 16

STM image of the Ge(111) c2×8 surface, obtained at a sample bias of 2.5 V. A rectangular unit cell is shown in the center of the image. The arrows indicate the presence of an extra row of adatoms, forming a local 2×2 structure. From [37], reproduced with permission.

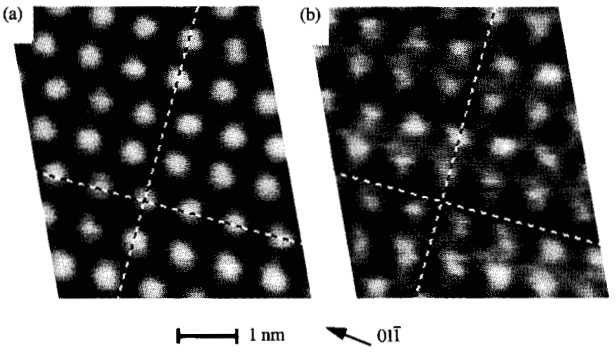

Figure 17

Voltage-dependent STM images of the Ge(111) c2×8 surface. The images were obtained at sample biases of (a) +1.2 V and (b) −1.2 V. Cross-hairs on the images are located at identical surface locations in (a) and (b). From [37], reproduced with permission.

surfaces [31, 39]) can be used to conclusively distinguish between these structures [40]. The results are shown in **Figures 17(a)** and **17(b)**, where two STM images are shown that were obtained at sample biases of +1.2 and −1.2 V, respectively. Cross-hairs on the images are located at identical surface locations. The corrugation maxima observed at positive bias correspond to the adatoms, as seen in Figure 16. The occurrence of spatially shifted maxima at negative bias indicates the existence of additional dangling bonds on the surface, located in this case on the surface layer beneath the adatoms. In the simple adatom model for this structure, shown in Figure 15(c), there are so-called *rest atoms* in the underlying layer, and the arrangement of these rest atoms agrees exactly with the corrugation maxima observed with negative bias. Alternatively, in the dimer-adatom-stacking-fault (DAS) model for this structure, no dangling bonds are present in the rest-atom layer [41], so that only the adatoms at *both* positive and negative bias should be observed, in contradiction to Figure 17.

Large-scale STM imaging can be used to characterize disorder and defect-related phenomena (e.g., atomic steps) on a surface. The width of the c2×8 domains we observe is about 500 Å. **Figure 18** shows an STM image that contains several such domains. An atomic step extends through the lower right-hand corner of the figure. Near the step edge, the formation of c2×8 is inhibited, and other atomic arrangements such as triangular regions of a 2×2 structure can be seen. The atomic step is a portion of the perimeter of a bilayer-deep "hole" on the surface (the step curves around and forms a closed loop). **Figure 19** shows a relatively large-scale STM image of the surface, exhibiting numerous such bilayer-deep holes. The holes result from the existence of adatoms on the surface, which gives the c2×8 structure a 12.5% greater surface atom density than that of an ideal bilayer of the cleaved surface. Thus, to form the c2×8 structure, additional atoms are required. On large flat terraces, this need for more atoms leads to the formation of bilayer-deep holes in the surface, as previously observed on the Si(111) surface [42]. The areal density of the holes observed in Figure 19 is found to be 9.8% ± 1.6% of the total image size, which is in fair agreement with the theoretical value of 12.5% for the simple adatom model. On the other hand, the DAS model for the c2×8 structure contains exactly the same number of atoms as an ideal bilayer [41], in disagreement with the above observations.

• *High-temperature imaging of atomic motion on the Ge(111) surface*

The image of a surface obtained at an elevated temperature frequently depends on the initial condition of the surface. For example, observations of single-atom diffusion on a surface require the presence of a nonequilibrium concentration of isolated atoms on the surface (which can be placed there by deposition at a lower temperature). For the case we are considering here, the Ge(111) c2×8

surface, portions which are perfectly ordered are found to remain stable up to temperatures of about 300°C (at which point the surface is known to undergo a phase transition into a disordered state [43]). Alternatively, if we image disordered features on the surface such as domain boundaries, where vacancies occur which can provide spaces into which adjacent atoms can move, we can observe atomic motion at temperatures as low as 150°C.

Figure 20 shows two images obtained from a Ge(111) surface at a temperature of 160°C. After preparation in a UHV system, a small amount of residual gas was allowed to adsorb onto the surface at high temperature, thus forming a disordered arrangement of adatoms. Small domains of 2×2 and c2×4 stacking arrangements can be seen in Figure 20, separated by numerous domain boundaries. Residual defects act to pin some atoms on the surface, thus enforcing this disordered state [44]. The remaining atoms appear to be in a perpetual state of motion, trying to achieve an optimal stacking arrangement on the surface. Figures 20(a) and 20(b) show two consecutive STM images, taken about 30 seconds apart. Considerable atomic motion has occurred between the images, which is clearly evident in the difference image shown in Figure 20(c). The positions which are occupied by atoms in (a) but not in (b) appear as the dark regions, while those positions occupied in (b) but not in (a) appear as the light regions. Entire rows of adatoms have shifted from (a) to (b) along each of the equivalent $[01\bar{1}]$ directions. Occasionally the adatom rows are in motion during the STM imaging process, thus producing "fuzzy" lines in the images.

The two images shown in Figure 20 are members of a sequence of 300 images obtained from the same surface region at 160°C. The movement of individual adatoms or rows of adatoms appeared to have occurred between most of the images, and the mean time between hops of the adatoms could be roughly estimated as the 30-s duration between images. At a higher temperature, the adatoms appeared to move more rapidly. **Figure 21** shows four consecutive images, obtained from a Ge(111) surface at 220°C. In the upper half of each image the adatoms are pinned by defects and are relatively stable, and in the lower half of the images the adatoms appear to be in motion. Entire groups of atoms are seen to move from one image to the next, and some regions of the images are fuzzy. The motion of the atoms was too rapid to resolve in those regions; obtaining them at a slower rate caused the fuzzy regions to grow in size. Even where the motion was the most rapid, individual adatoms or rows of adatoms could be resolved in some images. The mean time between adatom hops could be estimated roughly as the time between line scans of the image, which was 30/128 = 0.23 s. Combining the above two estimates for the hopping times and assuming a pre-exponential term of

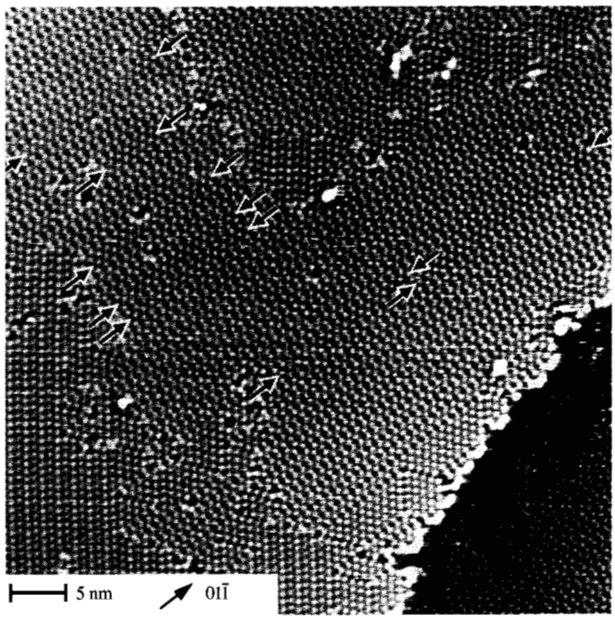

Figure 18

STM image of a Ge(111) surface, illustrating the domain structure of the c2×8 reconstruction. The image was obtained at a sample bias of 1.5 V. Extra rows of adatoms are indicated by the arrows. From [37], reproduced with permission.

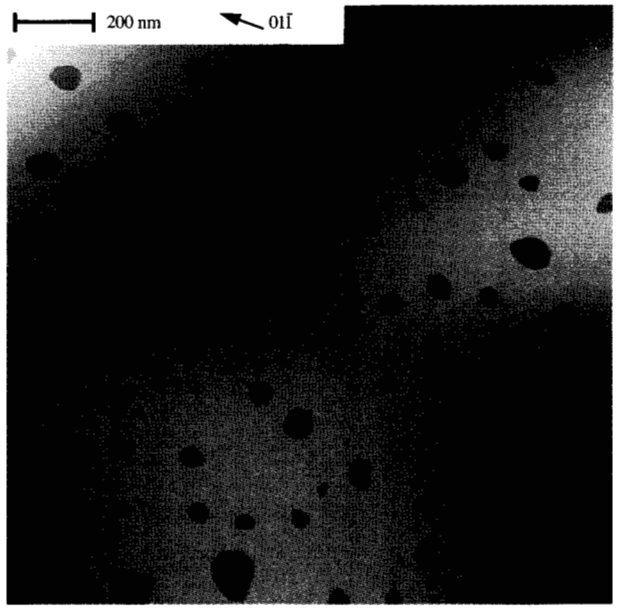

Figure 19

Large-scale STM image of a Ge(111) c2×8 surface, obtained at a sample bias voltage of 4.0 V. Bilayer-deep holes, appearing as dark regions, are formed because of the difference in surface atom density between the c2×8 and cleaved 2×1 structures. From [37], reproduced with permission.

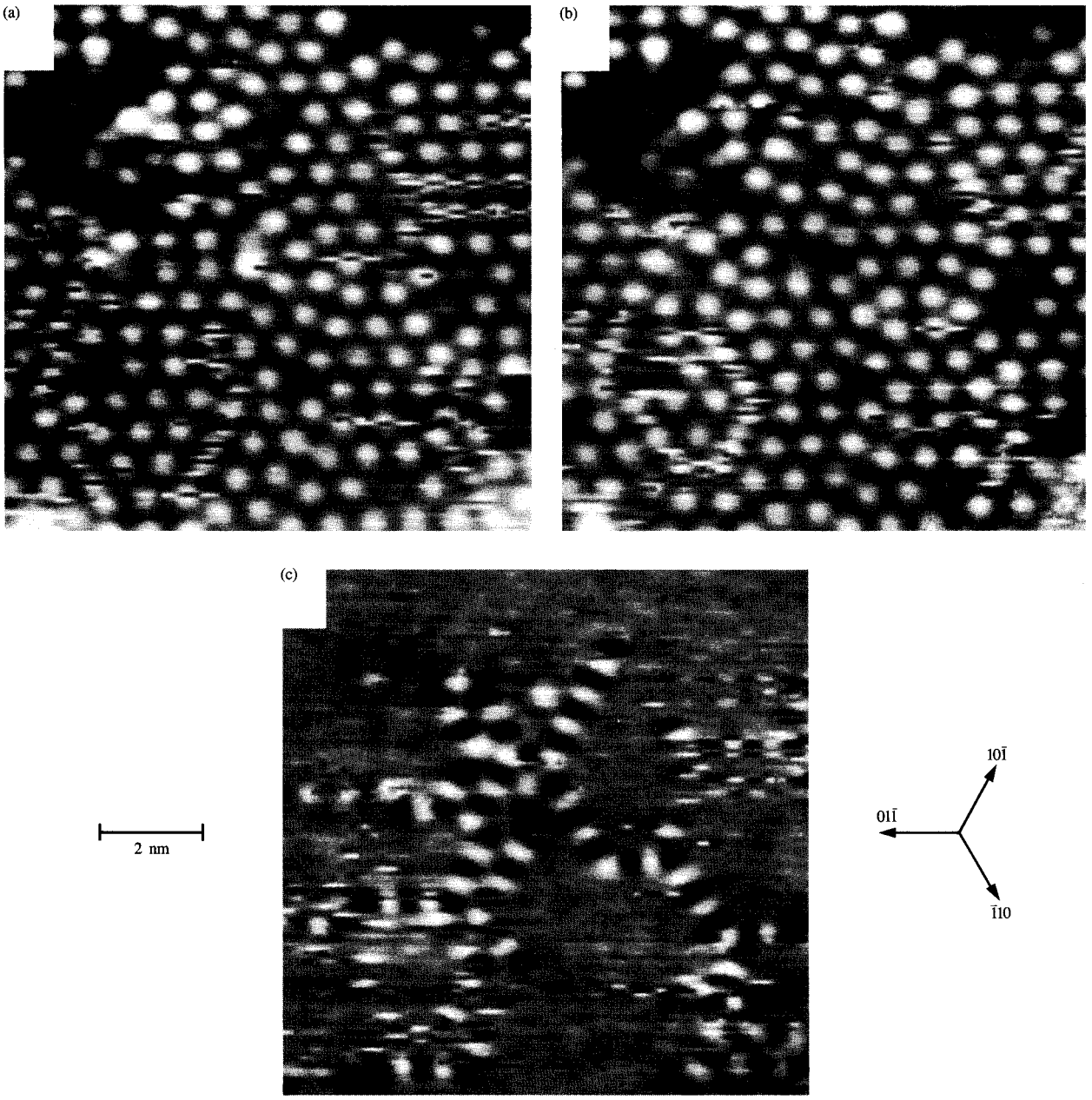

Figure 20

STM images of a Ge(111) surface containing a disordered arrangement of adatoms, introduced by residual gas adsorption at a high temperature. The images were obtained at 160°C and a sample bias of 1.5 V. Parts (a) and (b) are two consecutive images, taken 30 s apart. The difference between the images is shown in (c), indicating movement of adatom rows along the three equivalent [01$\bar{1}$] directions.

10^{12} s^{-1} yielded an activation energy of about 1.2 eV for the adatom motion.*

As the temperature was increased, the adatoms were found to move more rapidly, until they could no longer be resolved in the STM images. However, stable atomic arrangements continued to appear near step edges or other defects on the surface. Illustratively, **Figure 22** shows two consecutive images of a Ge(111) surface that were obtained at a temperature of 350°C. Atomic arrangements are clearly visible, indicative of the surface structure, which consists of unit cells, each containing two triangular half

*The estimated 1.2-eV activation energy actually applies to a combination of two processes—adatom motion and the formation of vacancies which provide space for the adatoms to move into. The latter process is probably the rate-limiting step.

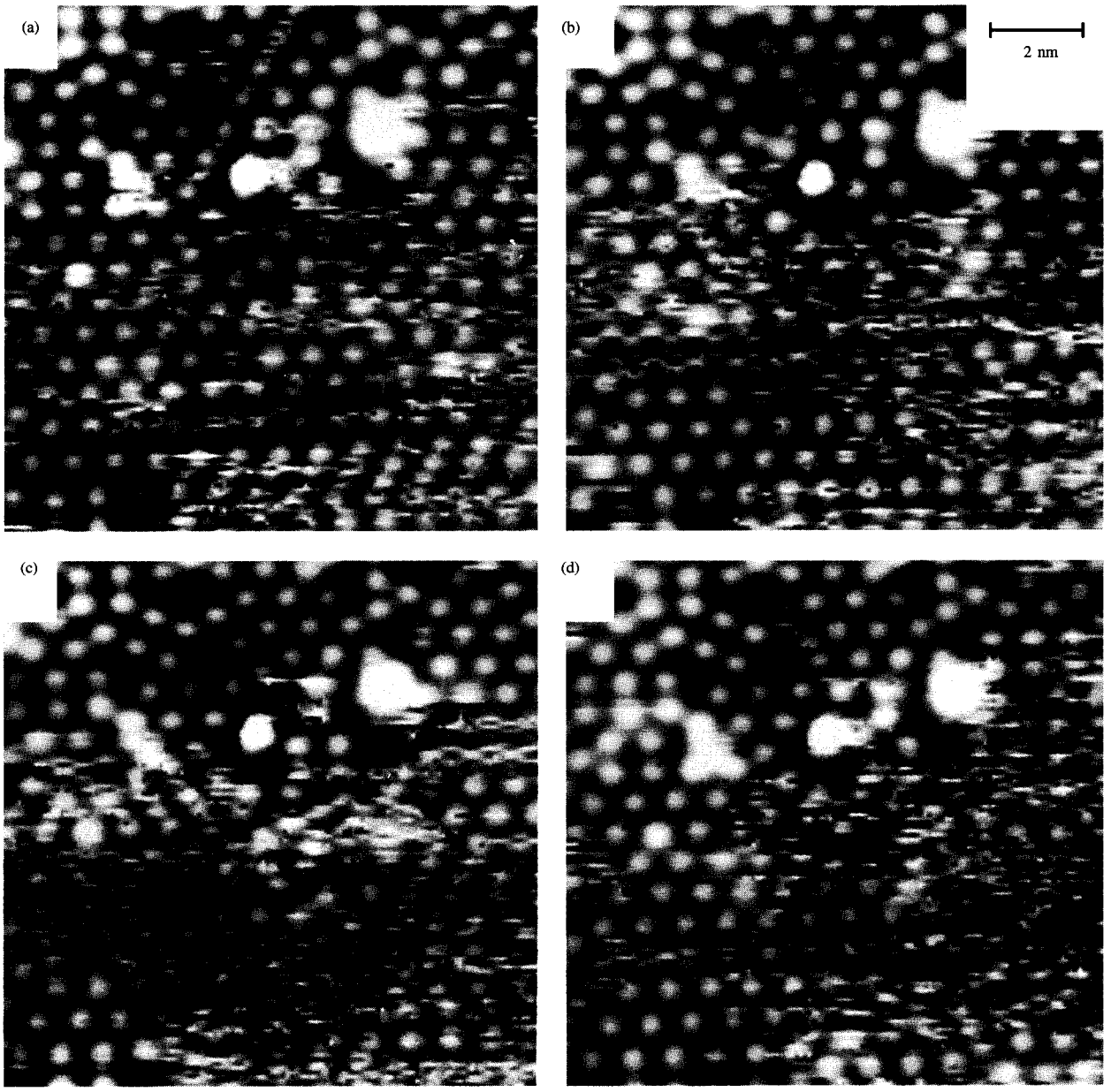

Figure 21

Four consecutive images of a Ge(111) surface at 220°C, obtained at a sample bias of 1.5 V. The images were taken 30 s apart. Considerable motion of the adatoms is evident in the lower half of each image.

unit cells. One half of a unit cell appears brighter than the other half; thus, this structure can be identified as a dimer-adatom-stacking-fault (DAS) 7×7 geometric arrangement [41, 45]. This arrangement is the well-known equilibrium structure of the Si(111) surface, but is unexpected for this Ge surface. Nevertheless, we commonly observe the 7×7 structure on the Ge(111) surface at temperatures of about 200°C and above, indicating that it is energetically favorable to form this structure on Ge at such temperatures.

In addition to the existence on the Ge(111) surface of the 7×7 structure, Figure 22 reveals that this structure changes dynamically at 350°C. The uppermost unit cell of the structure, which is seen in Figure 22(a), is clearly

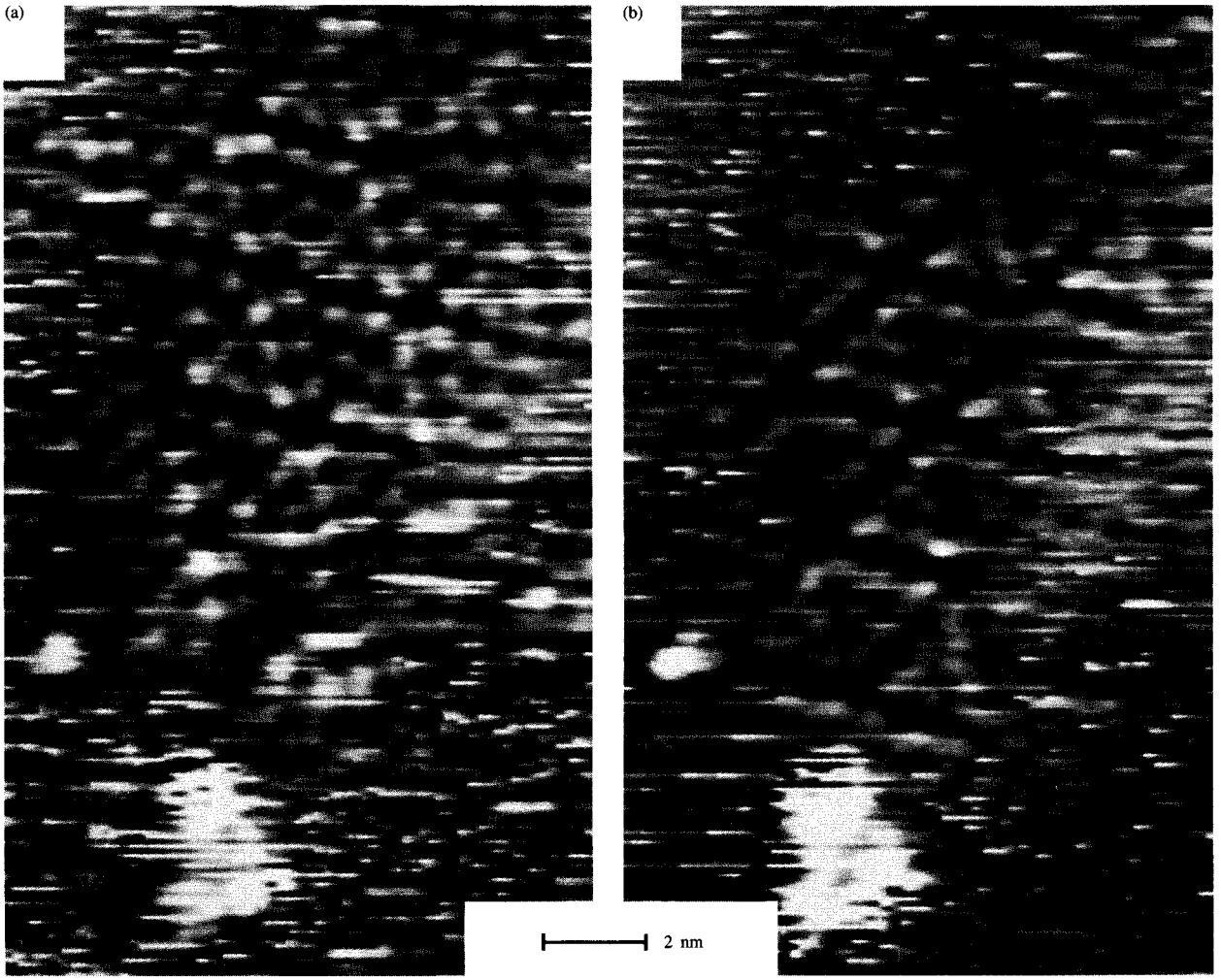

Figure 22

Two subsequent images of a Ge(111) surface at 350°C, obtained at a sample bias of −2.5 V. The images were taken 170 s apart. Domains of 7×7 structure are evident, with their size decreasing from (a) to (b).

absent in Figure 22(b). Subsequent images of this surface region also revealed changes in the size of the 7×7 domain, with the time between changes being of the order of the 170-s duration between images. As implied by its name, the DAS structure contains in addition to adatoms a *stacking fault* which affects the atom positions in the bilayer below the adatoms. The observed changes in the size of the 7×7 domain imply motion of these underlying atoms. With the above estimate of the time between configuration changes, and again assuming a pre-exponential factor of 10^{12} s^{-1}, we find an activation energy of about 1.8 eV. This energy now applies to the motion of the underlying layer of atoms, indicating that their motion requires more energy than does that of the adatoms.

• *Applications of STM to other semiconductor surfaces*

Scanning tunneling microscopy provides numerous methods for characterizing clean and metal-covered semiconductor surfaces. Associated spectroscopic methods are now well established; they yield the electronic structure of the surface, which in turn provides information on their geometric structure and chemical nature. Deposition and annealing processes on surfaces have been studied, with STM providing structural information from the atomic scale to the micron scale. High-temperature STM imaging has been shown here to be useful for exploring surface processes, such as single-atom diffusion and the formation of ordered structures. Acquiring images at different temperatures permits the

separation of different processes occurring on a surface, and the determination of microscopic details of the processes. Higher-speed STM imaging, currently under development, should be useful in further exploiting this ability to study surface dynamics.

The study of clean and metal-covered semiconductor surfaces in UHV constitutes the majority of semiconductor studies which have been performed with STM to date. Nevertheless, additional types of measurements are possible, and we briefly discuss some of those here. One application is in the study of actual semiconductor devices, probing, for example, potential profiles, concentration gradients, band offsets, and other properties of such devices. Major impediments to this type of study are the requirements of (a) preparing the devices in a clean (UHV) environment so that the tunneling characteristics are stable and reproducible, and (b) quickly and reproducibly positioning the STM probe tip over the desired portion of the device under question. Several groups have managed to overcome these impediments [46, 47], most notably Salemink and co-workers [48]. They studied AlGaAs/GaAs superlattices, cleaved in UHV and then imaged in cross section using STM. Positioning of the probe tip was accomplished *in situ* with a scanning electron microscope. Spectroscopic measurements were performed on either side of the AlGaAs/GaAs interface, revealing the variation in bandgap across the interface together with variations in the position of the Fermi level at the surface relative to the band edges.

Another application of STM which is difficult to implement is the modification of a surface under the influence of some tip-induced process. In addition to the requirements of stability and reproducibility, this application requires the development of a process for performing the "writing." Early work in this area included the localized exposing of resist films on a surface [49], and the localized deposition of metals by decomposition of organometallic molecules in the gas phase [50, 51]. Also, it was found that the probe tip can be used to create small indentations in a Si surface [52]. Two recent developments in the field of surface modification demonstrate a significant increase in reproducibility. The first of these has been reported by Mamin and co-workers, who have written 100-Å-diameter gold dots using a gold probe tip [53]. The writing was made possible primarily by the field-evaporation of atoms from the tip. The second development, reported by Eigler and co-workers, was performed at low temperatures on Xe atoms deposited on a Ni surface [54]. They found that careful and precise application of the bias between tip and sample enabled them to move individual Xe atoms across the Ni surface, making it possible to form lines and other patterns with the Xe atoms.

Medium-energy ion scattering

Medium-energy ion scattering (MEIS) is a technique for the determination of surface and interface structure [55], often complementary to the other techniques already discussed. The main advantages of MEIS are that 1) it provides quantitative information by virtue of well-characterized ion-scattering phenomena [56]; 2) it has high depth resolution, in particular close to the surface, where it can be used to carry out layer-by-layer structure determinations; 3) it has high elemental resolution, even to the extent that the isotopes of Ga can be clearly resolved in MEIS energy spectra [57], and 4) it can be used to assess crystal structure and quality and obtain a detailed determination of atomic positions at surfaces and near-surface interfaces. The main limitations of the technique are that it is an area-averaging technique (in contrast to the microscopy techniques discussed in previous sections), and that care must be taken to obtain data with sufficiently low ion beam doses to prevent sample damage. Recent developments in the parallel detection of scattered ions have greatly diminished the latter concern [57]. Finally, it should be noted that the experimental setup required to implement MEIS is rather complex and expensive, and not widely available.

An excellent general review of MEIS is available in the literature [55]. In this section we illustrate some of the above features with experimental results recently obtained in our laboratory.

- *Basics of MEIS*

Use is made of low Z ions in the energy range of 50 to 400 keV. The lower boundary is set by the scattering behavior, which becomes more complex and less well known at lower energies. Above roughly 50 keV the scattering is Rutherford-like, and the scattering cross sections are accurately known, permitting quantitative data analysis. In many cases the forte of MEIS is its high-energy resolution, made possible by the use of an electrostatic energy analyzer [58]. At 400 keV, the electrostatic field strength in the analyzer approaches 100 keV/cm, thus posing an upper limit on the ion energy. At an ion energy of 100 keV, the energy resolution is 120 eV, compared to 15 keV in a typical 2-MeV Rutherford backscattering (RBS) analyzer. This factor 100 advantage in energy resolution is crucial to obtaining superior depth and mass resolution. Conveniently, small ion accelerators in this energy range, with high energy stability, are available from several manufacturers.

Figure 23 shows the intensity of scattered ions obtained from the configuration shown in the inset [57] using a 200-keV He^+ incident beam, as a function of energy and scattering angle. The configuration consisted of a Si(111) substrate containing two embedded Ge quantum wells and an Sb monolayer adsorbed on the surface. The color scale

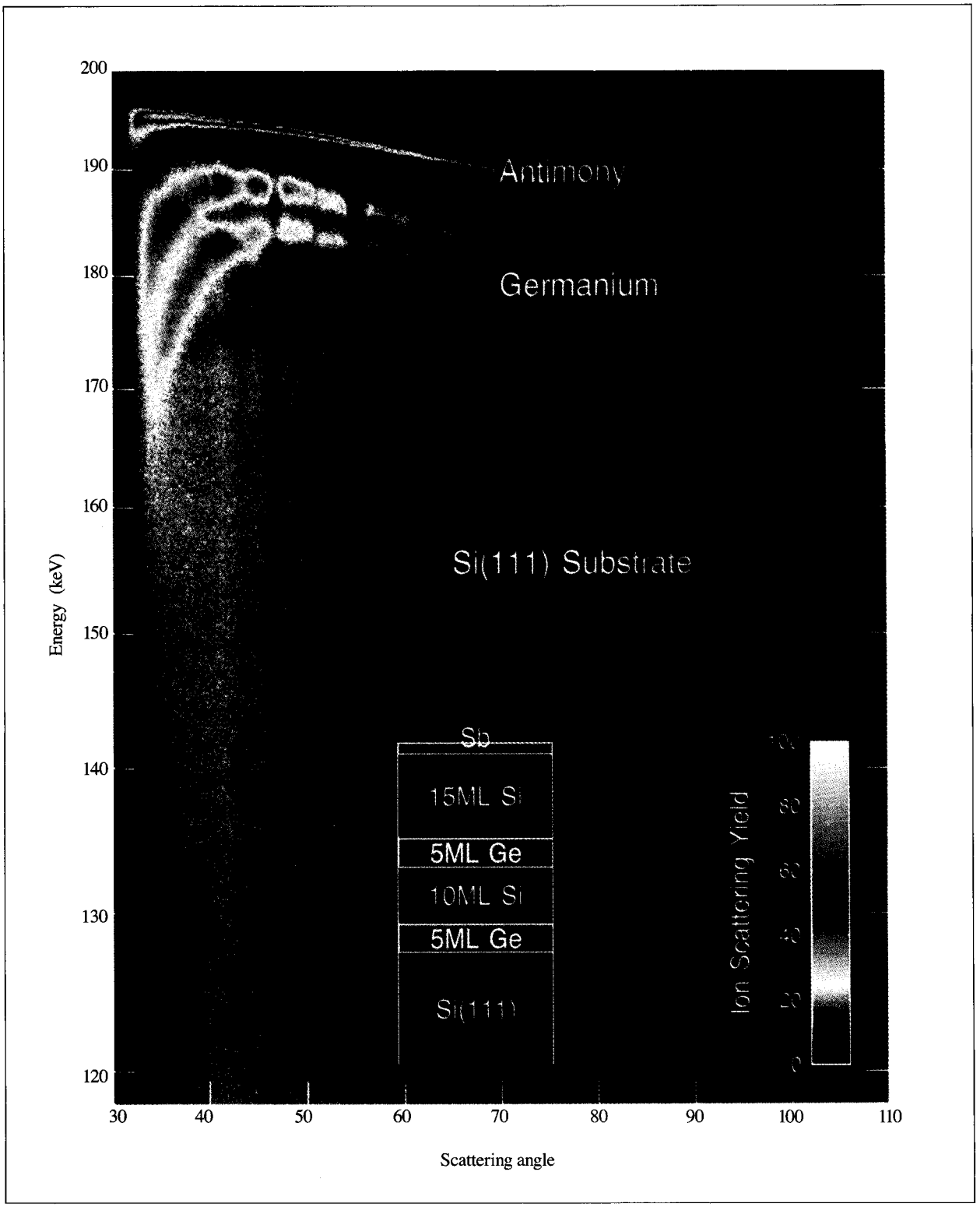

Figure 23

Ion-scattering energy spectra obtained using a 200-keV He^+ beam and a target consisting of a Si(111) crystal overgrown with an embedded double Ge quantum well and an overlying Sb monolayer. Mass separation is clearly observed, with the largest mass (Sb) showing up at the highest energies, and the smallest mass (Si) at lower energies. From [57], reproduced with permission.

encodes scattering intensity. The clear separation of the Sb, Ge, and Si signals is evident, as well as the dispersion of these signals with scattering angle. If an ion is scattered back into the vacuum upon colliding elastically with a target atom, its final energy is determined by conservation of energy and momentum. With increasing scattering angle, the ion is expected to lose more energy to the target atom. At a given scattering angle it loses more energy to a lighter target atom than to a heavier one, giving rise to elemental separation in the ion energy spectra. This separation increases at larger scattering angles, as can be seen in the figure.

The two Ge quantum wells give rise to two distinct energy bands. As an ion traverses a solid, it loses energy by inelastic electronic energy loss processes. This inelastic energy loss is proportional to distance traveled in the solid, related to depth by a simple geometric factor. The inelastic energy loss per nanometer peaks for many elements in the 50–400-keV ion energy range (for protons and He ions). A typical value of this energy loss would be 200 eV per nanometer of path length. This, together with the high-energy resolution of the scattering system used, results in a typical depth resolution of 2–3 Å in the near-surface region. Because of the statistical nature of the inelastic energy loss processes, this depth resolution degrades slowly with increasing depth. In Figure 23, the Ge signals curve downward to lower energy at the smallest scattering angles. This is due to a divergence of the path length traveled through the Si overlayer as the exit angle of the ions becomes more and more glancing, until all signal is cut off at the smallest scattering angles by the surface.

Additionally, the Ge and Si signals exhibit pronounced minima in scattering intensity at well-defined scattering angles. This is due to the so-called blocking effect. Ions scattered inside a crystal can reach the vacuum unless their outgoing path is blocked by other atoms. The atomic strings block the scattered ions very effectively and give rise to the observed minima. The angles at which these minima occur reveal the angles of the major crystal axes. The depths of the minima are a measure of crystal quality: The deeper the minima, the more perfect the crystal.

Frequently use is made of the channeling effect, in which the incoming ion beam is aligned with a major crystallographic direction. The first atoms in each atomic row cast a shadow cone onto their underlying atoms, shadowing them from the ion beam. Scattering is limited to atoms near the surface, and the scattering yield from the bulk is strongly reduced. Again, the magnitude of this reduction is a measure of crystal quality. Shadowing and blocking effects are not observed in amorphous or even polycrystalline samples (because of area averaging). To obtain the data shown in Figure 23, the ion beam was incident in a random direction, thus avoiding channeling effects and resulting in the highlighting of the blocking of the outgoing ions.

- *Ge–Si hetero-epitaxy on Si(111)*

The process by which atoms of one material are deposited on the surface of another crystalline material and assume the crystal structure and orientation of this substrate is referred to as (hetero-)epitaxial growth. Such growth results in intimate, even atomic contact over a large interfacial area. The epitaxial growth of layers of Ge on Si and of Si on Ge has been of interest recently. The growth of layers of Ge and Ge–Si alloys on Si has recently facilitated the fabrication of new and higher-performance semiconductor structures [59]. However, there are severe and fundamental problems to be overcome in that regard, deriving from the large (4.3%) difference in lattice constant between Si and Ge.

If Ge is deposited onto Si at 500°C to ensure epitaxial growth, it will initially wet the substrate, but after only three monolayers have been grown, Ge islands form, resulting in useless material [60]. The initial wetting occurs because Ge has a lower surface free energy than Si. Island formation follows because the lattice mismatch and its associated strain are too large in a uniform film. Growth of Si on Ge is more troublesome, because Si does not wet Ge, and islands form even at the lowest coverage.

The clean surfaces of Si and Ge contain a high density of dangling bonds, resulting from the reduced coordination of their surface atoms. The dangling bonds give rise to an extensive rearrangement of the atomic bonds in the surface to lower the surface energy. This situation can be changed by terminating the surface not with Si or Ge, but with a single atomic layer of an element having a different number of valence electrons, such as As or Sb [61]. In the ideal Si(111) surface, a surface atom should have three bonds to its underlying substrate. If the surface atom is Si, one valence electron should remain in a high-energy dangling-bond orbital. If the surface atom is As or Sb, two valence electrons should remain, filling a low-energy lone-pair orbital. Thus, As- or Sb-terminated Si and Ge surfaces are found to be extremely stable and chemically inert. High-quality epitaxial Ge films have been grown on an Sb-terminated Si(111) surface with no indication of island formation; the Sb monolayer was present during growth, and "floated" on the surface, retaining the surface energy at a low value [62].

Figure 24 shows ion-scattering energy spectra obtained from Si(111) samples containing thin Ge films that were grown without and with an Sb surface layer. First a six-monolayer-thick Ge film was grown at room temperature [Figure 24(a)]. Two Ge spectra are shown, in random incidence (dashed line) and in channeling incidence (solid line). The lack of reduction in scattering yield in the channeling geometry shows the lack of crystallinity in this

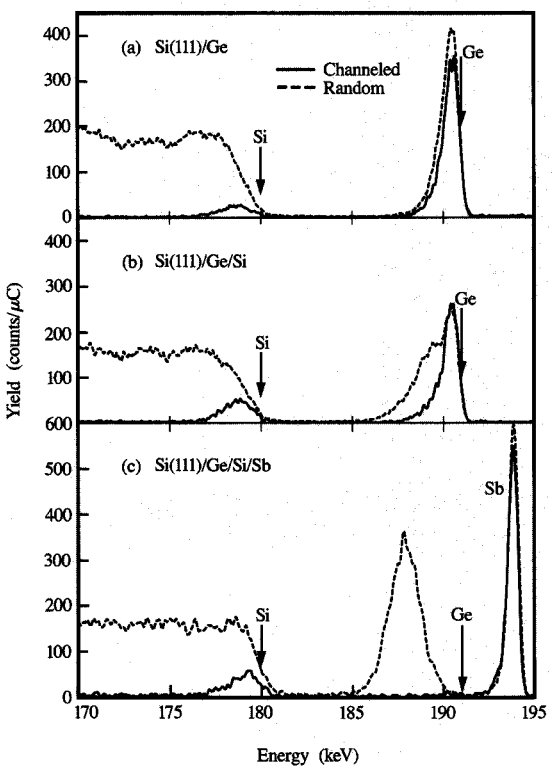

Figure 24

Backscattering spectra obtained, using a 200-keV He^+ beam, from targets consisting of Si(111) crystals and overlying, thin Ge films, in both random (dashed line) and channeling (solid line) beam incidence geometries: (a) with a 6-monolayer-thick Ge film deposited at room temperature; (b) with a 6-monolayer-thick Ge film deposited at 600°C; (c) with a 6-monolayer-thick Ge film deposited at 600°C in the presence of a monolayer of Sb, which acts to suppress Ge island formation.

film. From the compact shape of the Ge peak it appeared that the film was quite uniform in thickness. For a six-monolayer-thick film grown at 600°C, the spectrum looks very different [Figure 24(b)]. Now, there is a partial reduction in scattering yield in the channeling geometry, indicating crystallinity of the film. In the random spectrum, however, the Ge peak has a broad, low energy tail, indicating the presence of Ge islands, with an average thickness of 50 Å. As the ions travel through the islands they lose more energy inelastically than in a thinner, uniform film, giving rise to the tail. If a six-monolayer-thick film of Ge is deposited at 600°C on an Sb-terminated surface, the result is completely different [Figure 24(c)]: The Sb peak appears in the scattering spectrum (at higher energy because Sb has a higher atomic mass), and the Ge peak has the same compact shape as in Figure 24(a), indicating a uniform film thickness. In addition, the channeling spectrum shows a strong decrease in Ge scattering intensity because of the excellent crystal quality of the epitaxial Ge film. The Ge peak occurs at a somewhat lower energy than in Figures 24(a) and 24(b), because for (c) the Ge film was overgrown with a thin epitaxial Si film, which was also uniform in thickness and displayed excellent crystallinity.

Ge films that were grown with thicknesses of one to 100 monolayers using Sb termination were examined. The resulting ratio of channeling to random scattering intensity (commonly referred to as the "minimum yield," χ_{min}), a measure of crystal quality, is plotted in **Figure 25**. Initially, χ_{min} is very low, as expected for a high-quality epitaxial film. In fact, below a thickness of eight monolayers, the Ge films were pseudomorphic with the Si substrate. With increasing Ge film thickness the minimum yield increases rapidly, indicating a breakdown in crystal quality as misfit-strain-induced defects are injected into the film. Surprisingly, with increasing thickness, χ_{min} drops again, eventually to the same low value seen for very thin films, showing a recovery of crystal quality. Detailed investigations using TEM revealed that the increase of χ_{min} coincides with the injection of an interfacial misfit dislocation network, completely relieving misfit strain [62, 63]. Once this network is in place, the epitaxial film has the Ge lattice constant and can continue to grow without defects. Ion-scattering spectra obtained from the thick films showed an ion-scattering peak at the Ge–Si interface, related to the presence of dislocation strain fields.

- *The future of MEIS*

We have indicated how MEIS may be used to study epitaxial growth processes, *in situ*, with high resolution. The technique has been used to study a large range of phenomena, including surface relaxation and reconstruction, interface atomic structure and composition, surface melting, silicide formation, epitaxial growth in semiconductors and metals, oxidation and oxide removal, and polymer–metal interface formation and interdiffusion. The common attribute of MEIS for such studies has been that it can be used to obtain quantitative information with relative ease and with high depth resolution.

In our laboratory the use of MEIS is combined with the use of valence-band and core-level photoemission techniques, permitting an evaluation of the electronic and chemical structure of a sample under study. Detailed structural information may be obtained using high-resolution TEM after removal of the sample from its growth chamber. With the MEIS technique, on the other hand, epitaxial layers may be studied with high depth resolution directly in their growth chamber, and their growth may be continued after inspection. It is this

combination of depth and mass resolution, the capability of studying surface, interface, and crystal structure, the integration with other surface-analysis techniques, and the quantitative nature of the results obtained that make MEIS a unique and powerful technique. Although a decade ago it was available only at the Dutch FOM Institute in Amsterdam, about ten systems now exist worldwide, and its use is expected to increase.

Concluding remarks

Continued progress in microelectronics will rely more on the use of techniques for characterizing critical portions of device and circuit structures than in the past. Tighter control of manufacturing process and higher demands regarding reliability will require an increased understanding of associated materials-related aspects. The highly sensitive analysis techniques described here will likely play an important role in that effort. In the past decade we have seen the steady improvement of transmission electron microscopy, the rapid advancement of small probe techniques used in scanning transmission electron microscopy, and the emerging of scanning tunneling microscopy and the medium-energy ion-scattering technique. To meet the challenges ahead, it is anticipated that these techniques will evolve toward more automation for data acquisition, more versatility for studying a wide variety of materials in different ambients, and more flexibility for *in situ* observations.

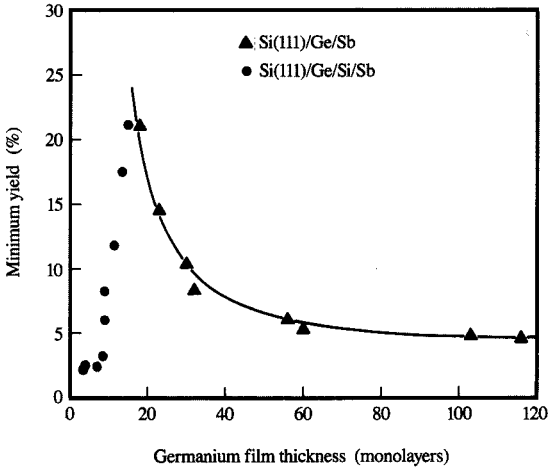

Figure 25

Minimum yield (ratio of channeling to random scattering geometry) for thin Ge films grown at 610°C in the presence of a monolayer of Sb. The increase of the minimum yield at an 8-monolayer Ge thickness is indicative of a rapid deterioration of crystal quality. At larger thicknesses the quality improves because of self-annihilation of lattice mismatch defects. From [62], reproduced with permission.

References

1. J. C. H. Spence, *Experimental High-Resolution Electron Microscopy*, 2nd ed., Oxford University Press, New York, 1988.
2. *High-Resolution Transmission Electron Microscopy and Associated Techniques*, P. Buseck, J. Cowley, and L. Eyring, Eds., Oxford University Press, New York, 1988.
3. T. S. Kuan and S. S. Iyer, *J. Appl. Phys.* **59**, 2242 (1991).
4. A. Ourmazd and J. C. Bean, *Phys. Rev. Lett.* **55**, 765 (1985).
5. F. K. LeGoues, V. P. Kesan, and S. S. Iyer, *Phys. Rev. Lett.* **64**, 40 (1990).
6. F. K. LeGoues, V. P. Kesan, S. S. Iyer, J. Tersoff, and R. Tromp, *Phys. Rev. Lett.* **64**, 2038 (1990).
7. J. L. Martins and A. Zunger, *Phys. Rev. Lett.* **56**, 1400 (1986).
8. T. O. Sedgwick, M. Berkenblit, and T. S. Kuan, *Appl. Phys. Lett.* **54**, 2689 (1989).
9. T. O. Sedgwick and P. D. Agnello, *Proceedings of the 11th International Conference on CVD*, K. E. Spear and G. W. Cullen, Eds., The Electrochemical Society, Pennington, NJ, 1990, p. 254.
10. K. C. Bretz, T. S. Kuan, P. D. Agnello, and T. O. Sedgwick, *Proceedings of the 49th Annual Meeting of the Electron Microscopy Society of America*, San Francisco Press, Inc., 1991, p. 798.
11. S.-F. Chuang, T. S. Kuan, and M. Pomerantz, *Proceedings of the 49th Annual Meeting of the Electron Microscopy Society of America*, San Francisco Press, Inc., 1991, p. 1052.
12. H. Chanzy, T. Folda, P. Smith, K. Gardner, and J.-F. Revol, *J. Mater. Sci. Lett.* **5**, 1045 (1986).
13. E. L. Thomas, *Proceedings of the 45th Annual Meeting of the Electron Microscopy Society of America*, San Francisco Press, Inc., 1987, p. 422.
14. M. Tsuji, in *Comprehensive Polymer Science*, Vol. 1, C. Booth and C. Price, Eds., Pergamon Press, Oxford, 1989, p. 785.
15. A. V. Crewe and J. Wall, *J. Molec. Biol.* **48**, 375 (1970).
16. A. V. Crewe, J. P. Langmore, and M. S. Isaacson, in *Physical Aspects of Electron Microscopy and Microbeam Analysis*, B. M. Siegel and D. R. Beaman, Eds., John Wiley & Sons, New York, 1975, p. 47.
17. P. E. Batson, in *Analytical Techniques for Thin Films, Treatise on Materials Science and Technology*, Vol. 27, K. N. Tu and R. Rosenberg, Eds., Academic Press, Inc., Boston, 1988, pp. 337–384.
18. S. J. Pennycook and D. E. Jesson, *Phys. Rev. Lett.* **64**, 938 (1990).
19. D. H. Shin, E. J. Kirkland, and J. Silcox, *Appl. Phys. Lett.* **55**, 2456 (1989).
20. P. E. Batson, *Rev. Sci. Instrum.* **57**, 43 (1986), and *Rev. Sci. Instrum.* **59**, 1132 (1988).
21. P. E. Batson, K. L. Kavanagh, J. M. Woodall, and J. W. Mayer, *Phys. Rev. Lett.* **57**, 2729 (1986).
22. P. E. Batson, K. L. Kavanagh, C. Y. Wong, and J. M. Woodall, *Ultramicrosc.* **22**, 89 (1987).
23. L. Dori, J. Bruley, D. DiMaria, P. E. Batson, J. Tornello, and M. Arienzo, *J. Appl. Phys.* **69**, 2317 (1991).
24. X. Weng, P. Rez, and P. E. Batson, *Solid State Commun.* **74**, 1013 (1990).
25. H. Ma, S. H. Lin, R. W. Carpenter, and O. F. Sankey, *J. Appl. Phys.* **68**, 288 (1990).
26. P. E. Batson and J. Bruley, *Phys. Rev. Lett.* **67**, 350 (1991).

27. P. E. Batson, *Phys. Rev. B* **44**, 5556 (1991).
28. S. G. Louie and M. L. Cohen, *Phys. Rev. B* **13**, 2461 (1976).
29. R. S. Becker, J. A. Golovchenko, D. R. Hamann, and B. S. Swartzentruber, *Phys. Rev. Lett.* **55**, 2032 (1985).
30. R. J. Hamers, R. M. Tromp, and J. E. Demuth, *Phys. Rev. Lett.* **56**, 1972 (1986).
31. J. A. Stroscio, R. M. Feenstra, and A. P. Fein, *Phys. Rev. Lett.* **57**, 2579 (1986).
32. U. Köhler, J. E. Demuth, and R. J. Hamers, *J. Vac. Sci. Technol. A* **7**, 2860 (1989).
33. A. J. Hoeven, J. M. Lenssinck, D. Dijkkamp, E. J. van Loenen, and J. Dieleman, *Phys. Rev. Lett.* **63**, 1830 (1989).
34. Y.-W. Mo, D. E. Savage, B. S. Swartzentruber, and M. G. Lagally, *Phys. Rev. Lett.* **65**, 1020 (1990).
35. M. O. Watanabe, K. Tanaka, and A. Sakai, *J. Vac. Sci. Technol. A* **8**, 327 (1990).
36. R. M. Feenstra and M. A. Lutz, *J. Vac. Sci. Technol. B* **9**, 716 (1991).
37. R. M. Feenstra and A. J. Slavin, *Surf. Sci.* **251/252**, 401 (1991).
38. R. S. Becker, J. A. Golovchenko, and B. S. Swartzentruber, *Phys. Rev. Lett.* **54**, 2678 (1985).
39. R. M. Feenstra, J. A. Stroscio, J. Tersoff, and A. P. Fein, *Phys. Rev. Lett.* **58**, 1192 (1987).
40. R. S. Becker, B. S. Swartzentruber, J. S. Vickers, and T. Klitsner, *Phys. Rev. B* **39**, 1633 (1989).
41. K. Takayanagi and Y. Tanishiro, *Phys. Rev. B* **34**, 1034 (1986).
42. R. M. Feenstra and M. A. Lutz, *Phys. Rev. B* **42**, 5391 (1990).
43. R. J. Phaneuf and M. B. Webb, *Surf. Sci.* **164**, 167 (1985).
44. T. Klitsner, R. S. Becker, and J. S. Vickers, *Phys. Rev. B* **44**, 1817 (1991).
45. R. M. Tromp, R. J. Hamers, and J. E. Demuth, *Phys. Rev. B* **34**, 1388 (1986).
46. S. Kordić, E. J. van Loenen, D. Dijkkamp, A. J. Hoeven, and H. K. Moraal, *J. Vac. Sci. Technol. A* **8**, 549 (1990).
47. M. Tanimoto and Y. Nakano, *J. Vac. Sci. Technol. A* **8**, 553 (1990).
48. Q. Albrektsen, P. J. Arent, H. P. Meier, and H. W. M. Salemink, *Appl. Phys. Lett.* **57**, 31 (1990).
49. M. A. McCord and R. F. W. Pease, *J. Vac. Sci. Technol. B* **6**, 293 (1988).
50. E. E. Ehrichs, R. M. Silver, and A. L. de Lozanne, *J. Vac. Sci. Technol. A* **6**, 540 (1988).
51. M. A. McCord, D. P. Kern, and T. H. P. Chang, *J. Vac. Sci. Technol. B* **6**, 1877 (1988).
52. E. J. van Loenen, D. Dijkkamp, A. J. Hoeven, J. M. Lenssinck, and J. Dieleman, *J. Vac. Sci. Technol. A* **8**, 574 (1990).
53. H. J. Mamin, P. H. Guethner, and D. Rugar, *Phys. Rev. Lett.* **65**, 2418 (1990).
54. D. M. Eigler and E. K. Schweizer, *Nature* **344**, 524 (1990).
55. J. F. van der Veen, *Surf. Sci. Rep.* **5**, Nos. 5/6 (1985).
56. W. K. Chu, J. W. Mayer, and M. A. Nicolet, *Backscattering Spectrometry*, Academic Press, Inc., New York, 1978.
57. R. M. Tromp, M. Copel, M. C. Reuter, M. Horn von Hoegen, J. Speidel, and R. Koudijs, *J. Phys. E: Sci. Instrum.* **62**, 2679 (1991).
58. R. G. Smeenk, R. M. Tromp, H. H. Kersten, A. J. H. Boerboom, and F. W. Saris, *Nuclear Instrum. & Meth.* **195**, 581 (1982).
59. See for example *New Heterostructures on Silicon: One Step Further with Silicon*, Y. I. Nissim and E. Rosencher, Eds., Kluwer Academic Publishers, Dordrecht, 1989.
60. P. M. Maree, K. Nakagawa, F. M. Mulders, and J. F. van der Veen, *Surf. Sci.* **191**, 305 (1987).
61. R. D. Bringans, R. I. G. Uhrberg, M. A. Olmstead, and R. Z. Bachrach, *Phys. Rev. B* **34**, 7447 (1986).
62. M. Horn-Von Hoegen, F. K. LeGoues, M. W. Copel, M. C. Reuter, and R. M. Tromp, *Phys. Rev. Lett.* **67**, 1130 (1991).
63. F. K. LeGoues, R. M. Tromp, M. Horn-von Hoegen, and M. W. Copel, *Phys. Rev. B* **44**, 12894 (1991).

Received November 7, 1991; accepted for publication May 19, 1992

Tung-Sheng Kuan *IBM Research Division, Thomas J. Watson Research Center, P.O. Box 218, Yorktown Heights, New York 10598 (KUAN at YKTVMZ, kuan@watson.ibm.com).* Dr. Kuan received his B.S. degree in physics from National Taiwan University in 1970, and his M.S. and Ph.D. degrees in materials science from Cornell University in 1974 and 1977, respectively. He joined the device materials group at the IBM Thomas J. Watson Research Center as a Research Staff Member in 1977. Since then his research activities have involved the development and application of high-resolution electron microscopy and diffraction techniques to studies of defects, interfaces, materials processing, and structure-properties correlations. In 1989 he received an IBM Outstanding Innovation Award for his work on long-range ordering in semiconductor alloys. He currently manages the Interconnection Materials and Modeling group in the System Technology and Science Department at the Thomas J. Watson Research Center. Dr. Kuan is a member of the American Physical Society, the Materials Research Society, the Minerals, Metals, and Materials Society, and the Electron Microscopy Society of America.

Philip E. Batson *IBM Research Division, Thomas J. Watson Research Center, P.O. Box 218, Yorktown Heights, New York 10598 (BATSON at YKTVMZ, batson@watson.ibm.com).* Dr. Batson received a B.S. degree in engineering physics from Cornell University in 1970, and a Ph.D. in applied physics in 1976. From 1976 until 1978 he was employed by Glasgow University as a Research Fellow to evaluate new techniques in scanning transmission electron microscopy (STEM). During this time he was based at the Cavendish Laboratory in Cambridge, England. Since December 1978 he has been employed by IBM as a Research Staff Member. From December 1978 until February 1980, he was also a Visiting Fellow at Cornell University. His recent research has included investigation of size effects in inelastic electron scattering in very small volumes. This work includes investigation of interband absorption at defects in semiconductors, surface plasmon resonances in complicated shapes, and core excitonic distortion in spatially resolved electron energy loss scattering.

Randall M. Feenstra *IBM Research Division, Thomas J. Watson Research Center, P.O. Box 218, Yorktown Heights, New York 10598 (FEENSTRA at YKTVMZ, feenstra@watson.ibm.com).* Dr. Feenstra is a Research Staff Member in the System Technology and Science Department at the Thomas J. Watson Research Center. He received a B.Ap.Sc. degree in engineering physics in 1978 from the University of British Columbia, and a Ph.D. degree in applied

physics in 1982 from the California Institute of Technology. Dr. Feenstra joined IBM in 1982, and since then has used scanning tunneling microscopy (STM) to study semiconductor surfaces and interfaces. For his work in STM, Dr. Feenstra has received an IBM Outstanding Innovation Award and the Peter Mark Memorial Award from the American Vacuum Society. He is a member of the American Physical Society and the American Vacuum Society.

Alan J. Slavin *Department of Physics, Trent University, Peterborough, Ontario K9J 6Y3, Canada (aslavin@trentu.ca).* Professor Slavin received his B.A.Sc. in engineering science in 1967 and his M.Sc. in physics in 1968, both from the University of Toronto, and his Ph.D. in physics from Cambridge University in 1971. He then held an NSERC postdoctorate fellowship at McMaster University before moving in 1973 to Trent University, where he is currently Chairman of the Department of Physics. He has recently been a visiting scientist at the IBM Thomas J. Watson Research Center, working with Dr. Feenstra in scanning tunneling microscopy. Professor Slavin's current research interests are in the structure and chemical properties of solid surfaces. He is a member of the Canadian Association of Physicists, the American Vacuum Society, and both the Ontario and American Associations of Physics Teachers.

Ruud M. Tromp *IBM Research Division, Thomas J. Watson Research Center, P.O. Box 218, Yorktown Heights, New York 10598 (TROMP at YKTVMZ, tromp@watson.ibm.com).* Dr. Tromp is Manager of Interface Science at the IBM Thomas J. Watson Research Center. He received his Ph.D. in physics in 1982 from the University of Utrecht. In his thesis work at the FOM Institute for Atomic and Molecular Physics in Amsterdam he used medium-energy ion scattering for the study of semiconductor surface structures. He joined IBM in 1983. His research interests are in interface physics, in particular *in situ* studies of epitaxial growth phenomena, involving the use of techniques such as scanning tunneling microscopy (STM), transmission electron microscopy (TEM), low-energy electron microscopy (LEEM), and medium-energy ion scattering (MEIS). Dr. Tromp received the Wayne B. Nottingham Prize at the 1981 Conference on Physical Electronics, an IBM Outstanding Innovation Award for his work in scanning tunneling spectroscopy in 1987, and an IBM Outstanding Innovation Award for his work on surfactant-mediated epitaxial growth in 1991. He is a member of the American Physical Society and the Materials Research Society.